Ralf Gamillscheg

Effects of Non-Magnetic Impurities on the Two-Leg Ladder Compound $SrCu_2O_3$

DIPLOMARBEIT
zur Erlangung des akademischen Grades
Diplom-Ingenieur
der Studienrichtung Technische Physik

Technische Universität Graz

Betreuer:
Ao. Univ.-Prof. Hans-Gerd Evertz
Institut für Theoretische Physik - Computational Physics

Graz, Oktober 2006

Abstract

$SrCu_2O_3$ is a prominent representative of a class of materials with intriguing quasi-1-dimensional properties. It consists of weakly coupled CuO ladders and is closely related to high temperature superconductors. The discovery of a spin-gap in this material has triggered a large amount of experimental and theoretical research. Most magnetic properties have been successfully described by a simple spin-1/2 Heisenberg model on a single ladder. Experiments with doping of a small amount of nonmagnetic Zn atoms in place of Cu have however observed surprisingly large changes in magnetic properties, including a phase transition to an ordered system at low temperature.

In this thesis, the physics of the Zn-doped material is examined with the help of Quantum Monte Carlo (QMC) calculations and with the Density Matrix Renormalization Group (DMRG). The material is described by an extended Heisenberg model with vacancies at the location of the Zn atoms. They induce effective non-local spin-1/2 degrees of freedom. The analysis of magnetization profiles, excitation spectra, and correlations delivers information about doping effects. Simulation of NMR spectra shows that the drastic broadening observed experimentally at small temperatures is caused by physics beyond the Heisenberg model studied.

By including the coupling between stacked ladders, a quantum phase transition is induced. The quantum critical properties of this transition are studied and shown to be compatible with the $O(3)$ Heisenberg model.

Zusammenfassung

$SrCu_2O_3$ ist ein Vertreter einer Klasse von Materialien, die so genannte quasi-1-dimensionale quantenmechanische Eigenschaften besitzen. Es besteht aus schwach gekoppelten CuO-Leitern und ist nahe verwandt mit einigen Hochtemperatur-Supraleitern. Nach Entdeckung eines Spingaps in dem Material rückte es in den Mittelpunkt des Interesses vieler experimenteller und theoretischer Arbeiten. Die meisten magnetischen Eigenschaften konnten erfolgreich mit einem einfachen Spin-1/2 Heisenberg-Modell einfacher Leitern beschrieben werden. Doch die Dotierung des Materials mit Zn Atomen anstelle von Cu zeigte in den Experimenten eine überraschend große Änderung der magnetischen Eigenschaften, einschließlich eines Phasenübergangs zu einem geordneten System bei niedrigen Temperaturen.

In der vorliegenden Arbeit wird die Physik des Zn-dotierten Materials mit Hilfe von Quanten-Monte-Carlo (QMC) sowie der Dichtematrix-Renormierungsgruppe (DMRG) untersucht. Das Material wird dabei mit einem erweiterten Heisenberg-Modell mit Leerstellen an den Positionen der Zn-Atome beschrieben, welche effektive, nicht-lokale Spin-1/2 Freiheitsgrade induzieren. Die Auswertung von Magnetisierungsprofilen, Anregungsspektren und Korrelationen liefert Einblick in die Auswirkungen der Dotierung. Simulationen von NMR-Spektren zeigen, dass die in den Experimenten beobachtete starke Verbreiterung des Spektrums bei kleinen Temperaturen nur mit Physik erklärt werden kann, die über das Heisenberg-Modell hinausgeht.

Bei zusätzlicher Beachtung der Kopplungen der Leitern untereinander taucht ein Quantenphasenübergang auf. Dessen quantenkritische Eigenschaften werden untersucht und es wird gezeigt, dass er einem Phasenübergang des $O(3)$-Heisenberg-Modells entspricht.

Contents

1 Basics

1.1 Introduction

1.1.1 The Material $SrCu_2O_3$

An investigation of $SrCu_2O_3$ may lead to better understanding of effects in a whole class of materials. Many representatives of the so-called *cuprates* exhibit superconducting behavior, which is connected to intriguing quantum-mechanical effects also seen in the material at hand.
It is known that $SrCu_2O_3$ crystallizes in a ladder-type form, where the Cu-atoms represent the elements constructing the ladders (fig. 1.1). The O-atoms mediate the electron exchange between the Cu-atoms, while the Sr-atoms are located between the Cu-layers. In literature ladders are usually denoted as quasi-1-dimensional objects, which expresses the appearance of interesting quantum effects at the cross-over of one- and two-dimensionality.
Although the interaction along the legs and rungs are widely considered to be dominating the behavior of the system, further couplings in directions inside and connecting the ladders may have large influence on the material's properties.

1.1.2 Spin-Ladders

The dominating part of the magnetic effects in the material are the unpaired electrons in the valence shell of the Cu-atoms. So a possible simulation of magnetic properties can rely on a model where each of these atoms is replaced by a single spin-1/2. Together with the specific crystallization pattern of $SrCu_2O_3$ this leads to a possible description with the help of spin-ladders.
Such simple systems of spins have been the focus of many works in the past years and were examined using many different techniques. A prominent representative is the *Heisenberg chain* which is a line of consecutive sites with couplings only between

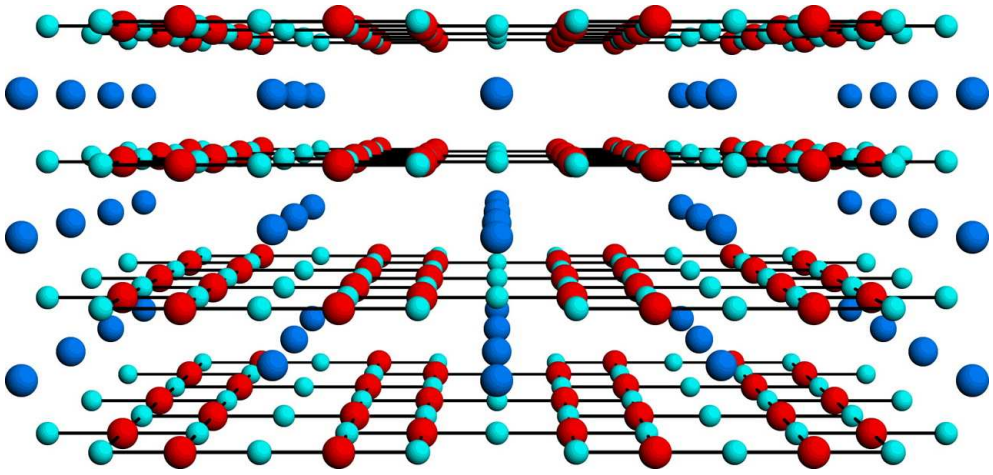

Figure 1.1: 3D picture of $SrCu_2O_3$ crystallization (from [7]). Red: Cu, light blue: O, dark blue: Sr. The ladder structure can be seen inside the planes which are stacked above another. The Cu-atoms form the ladders and the O-atoms mediate the interaction between them.

neighbouring spins (see sec. 1.2.1). This rather simple quantum mechanical system exhibits critical behaviour, expressing itself in a polynomial decay of correlations along the chain, referred to as anti-ferromagnetic long range order (ALRO). Accordingly, the correlation length is infinite.

$$G(r) \propto \frac{1}{r}, \qquad \xi = \infty \tag{1.1}$$

It is possible to treat such a problem analytically with the so-called Bethe ansatz [8].
The *Heisenberg ladder* can be seen as two coupled chains with an additional parameter $J_\perp$ determining the inter-chain interaction. For large values of $J_\perp$ the spins on each rung of the ladder form a singlet (see sec. 1.3). This leads to a finite singlet-triplet spin-gap and a finite correlation length. It came as a surprise that even at very small inter-chain couplings $J_\perp$ a finite spin-gap exists ($\propto J_\perp$) [9, 10].

$$G(r) \propto e^{-r/\xi}, \qquad \xi = 3.1(1) \tag{1.2}$$

Here the correlation length for the spatially isotropic ladder was given as an example for finite values of the characteristic length. The Heisenberg ladder is said to be in a *dimerized* phase with tendency to build *dimers* (see sec. 1.3).
Furthermore it is known that ladders with an even number of legs have finite correlation lengths and a spin-gap, but odd-legged ones have neither. The finite spin-gap of even-legged ladders decreases exponentially with the number of legs [1].

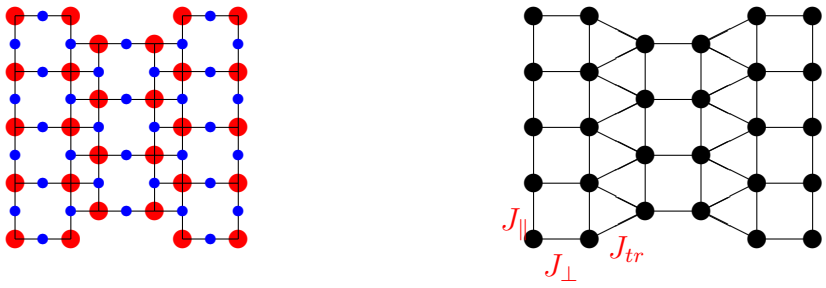

Figure 1.2: Left: The Cu-planes of $SrCu_2O_3$, red: Cu, blue: O. Right: The trellis lattice.

1.1.3 The Spin-Gap

The spin-gap is a physical measurable quantity describing the dynamics of a system. It is simply defined as the lowest energy needed to realise an elementary excitation. In those systems considered here these excitations are spin-waves, generally comprised of two so-called *spinons*. A spinon is essentially a moving domain wall, beyond it the anti-ferromagnetic spin configuration is reverted. The spinon carries a spin-1/2 and can be associated with a velocity and a dispersion relation [11].

1.1.4 Lattice Structure

There are different lattice types which may reflect the properties of the material $SrCu_2O_3$. The first approximation to nature is a simple ladder, whereas including inter-ladder couplings leads to more expensive numerical efforts. The two different couplings to neighboring ladders to be considered are the in-plane couplings and the couplings in the stacking direction. The in-plane couplings of $SrCu_2O_3$ are known to build a so-called trellis lattice where the inter-ladder bonds form a triangular configuration (see fig. 1.2). For the stacked interaction the ladders can simply be put site-by-site on top of each other (see fig. 1.3). This also has influence on possible numerical strategies because trellis lattices of anti-ferromagnetic systems give rise to the sign-problem in Monte Carlo simulations [12]. So this system can only be treated with other methods (e.g. DMRG, see sec. 1.8).

For each of these lattice types different coupling strengths for the interactions have to be defined (eg. $J_\parallel$, $J_\perp$, J_{tr}, and J_3; see fig. 1.2 and 1.3).

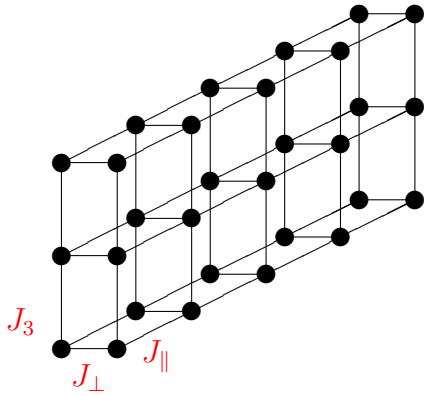

Figure 1.3: Stacked ladders.

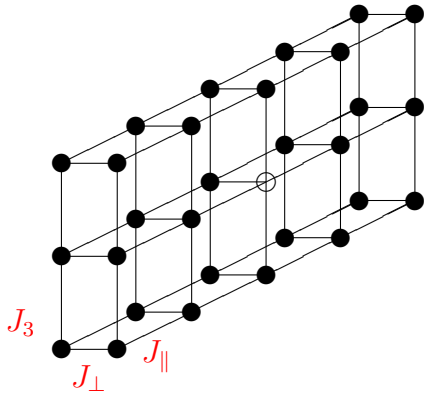

Figure 1.4: Stacked ladders with vacancy.

1.1.5 Doping with Non-Magnetic Impurities

A possibility of doping is replacing the Cu atoms by Zn atoms. This means inserting a vacancy into our naive model because all electrons in Zn are paired and no spin can be noticed from outside (see fig. 1.4). An unpaired spin is distributed in the surroundings of the vacancy according to the resonating valence-bond picture (see sec. 1.3). The spatial decay of the effect is strongly connected to the correlation length in the material [13].

1.1.6 Phase Transitions

In statistical mechanics phase transitions [14] are characterized by a singularity in one of the derivatives of the free energy. Phase transitions with singularities in the second derivatives only are said to be *continuous phase transitions*. They exhibit *critical be-*

haviour which means that the asymptotic conduct of important physical properties is defined by a small set of *critical exponents* alone. Also the asymptotic behaviour is said to be of polynomial style which expresses another important fact about phase transitions: *self-similarity* on all length scales. As a consequence many different systems can be classified in a few *universality classes* which all have the same set of critical exponents.
These critical exponents exist in flavours describing quantities such as specific heat (α), order parameter (β), susceptibility (γ), critical isotherm (δ), correlation length (ν), and greens function (η).
Quantum critical points are also characterized by a diverging amount of fluctuations, but in contrast to thermodynamics these fluctuations are not driven by the temperature but by a major property of quantum mechanics itself: the Heisenberg uncertainty principle. This leads to the important fact, that quantum critical phenomena occur at $T = 0$.
Although strictly speaking phase transitions are prerogatives of infinite systems not existing in nature or, in case of quantum critical points, defined for zero temperature not reachable in nature, the effects on observable systems are quite large and considerable changes in physical quantities deliver proof of their existence.
An important observable for characterizing two different phases is the *order parameter*. The magnitude of spatial fluctuations of the order parameter is expressed with the correlation length, which diverges at the critical point. In this thesis the physical observable describing the ordered phase is the magnetization.

1.2 The Model

1.2.1 The Heisenberg Model

The Heisenberg model describes the bulk material solely via interactions of spins on fixed sites. These quantum-mechanical spins are believed to be an accurate enough representation of the material's magnetic properties.
Starting from the Schrödinger equation of the bulk material some approximations have to be applied to be able to calculate the band-structure of the material as well as magnetic properties. A common approach uses the *local density approximation* (LDA), which usually neglects the effects of correlations and therefore corresponds largely to the local interactions of atoms. In the next step, the bands closest to the Fermi energy are approximated by a *tight-binding* model, i.e. an electron model that contains only hop-

pings but no other interactions. The resulting hopping amplitudes Δ_{ij}, together with estimates of Coulomb repulsions U_{ij}, provide an effective Hubbard type model. If there is exactly one interacting electron on the outer shell of each relevant atom the system is called *half-filled*. It can then be mapped perturbatively from a Hubbard model with hopping electrons to the Heisenberg model.
The Hamiltonian reads as follows:

$$H = J \sum_{\langle i,j \rangle} \left(\frac{1}{2} \left(S_i^+ S_j^- + S_i^- S_j^+ \right) + S_i^z S_j^z \right) + h \sum_i S_i^z \tag{1.3}$$

where J denotes the coupling strength, S_i the spin operators at site i and h a magnetic field. The triangle brackets $\langle i, j \rangle$ symbolize a sum over neighbouring sites only. With positive coupling constants this Hamiltonian describes an anti-ferromagnetic system with tendency to alternating signs of neighbouring spins. Note that the couplings of spin components in all three internal directions are equal. Within this thesis no anisotropy is introduced to the Heisenberg model if not stated otherwise.
Another interesting matter is the origin of anti-ferromagnetic couplings in the materials considered [15]. This can be understood by considering the Hubbard model which includes possible hoppings of electrons to neighbouring sites. In the latter it is easy to understand that a configuration of spins with different signs is favoured due to the possible hopping of one electron to the other's site which of course is only allowed for opposite signs. This consideration of Pauli's principle gives rise to anti-ferromagnetic couplings in the simpler Heisenberg model.

1.2.2 The Ring Exchange

The *cyclic exchange* or *4-spin ring exchange* term can be defined for plaquettes of four spins. It can be seen as the next order perturbation theory by considering possible effects of the exchange potential and it mediates a spin hopping clockwise or counter-clockwise around the plaquette. Mathematically expressed:

$$\begin{aligned} H_{cycl} &= J_{cycl} \sum_{plaquettes} 4 \Big[\left(\vec{S}_1 \cdot \vec{S}_2 \right) \left(\vec{S}_3 \cdot \vec{S}_4 \right) + \left(\vec{S}_1 \cdot \vec{S}_4 \right) \left(\vec{S}_2 \cdot \vec{S}_3 \right) \\ &- \left(\vec{S}_1 \cdot \vec{S}_3 \right) \left(\vec{S}_2 \cdot \vec{S}_4 \right) \Big] + \vec{S}_1 \cdot \vec{S}_2 + \vec{S}_2 \cdot \vec{S}_3 + \vec{S}_3 \cdot \vec{S}_4 \\ &+ \vec{S}_4 \cdot \vec{S}_1 + \vec{S}_1 \cdot \vec{S}_3 + \vec{S}_2 \cdot \vec{S}_4 + \frac{1}{4} \end{aligned} \tag{1.4}$$

where the spins $1 \ldots 4$ are arranged (anti-)clockwise around a plaquette [16].

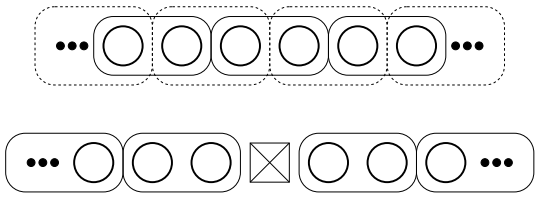

Figure 1.5: The resonating valence-bond (RVB) picture for the Heisenberg chain. Here the unperturbed chain has a doubly degenerate ground state (above), while the insertion of a vacancy leads to a fixation of dimers (below).

1.3 The Resonating Valence-Bond Picture (RVB)

A key picture for better understanding of the effects of doping onto a spin system is the resonating valence-bond description. It states that despite the long range correlations the local behavior of the spins is dominated by the formation of short spin singlets.

In a *Heisenberg chain* applying this picture leads to a doubly degenerate ground state where in the chain ABCDEF either A couples to B and C to D or B to C and D to E and so on (see fig. 1.5). Taking one spin out of the system means disturbing this degeneracy. Considering that in this simple picture one site resonates only with one of its neighbours the singlet states to the right and to the left side of the impurity are spatially fixed. Therefore it is not difficult to imagine that the correlations nearby are enhanced.

The *Heisenberg ladder* allows in principle for several possible dimerization patterns (fig. 1.6). While a strong coupling along the two chains of the ladder increases the building of singlets on the chains, strong rung-couplings lead to a preferred state of rung dimers. This ladder-typical spin-gapped state [17] is a property of the system for all finite inter-chain coupling strengths.

The insertion of vacancies on the ladder leaves an unpaired spin in the surroundings of the vacant site (see fig. 1.7). This picture will become handy to describe many effects of vacancy insertion.

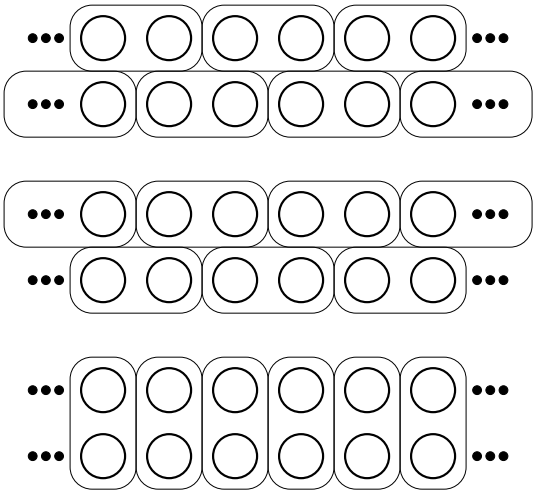

Figure 1.6: The resonating valence-bond (RVB) picture for the Heisenberg ladder. In principle several different dimerizations are possible, but some are preferred depending on the coupling anisotropy.

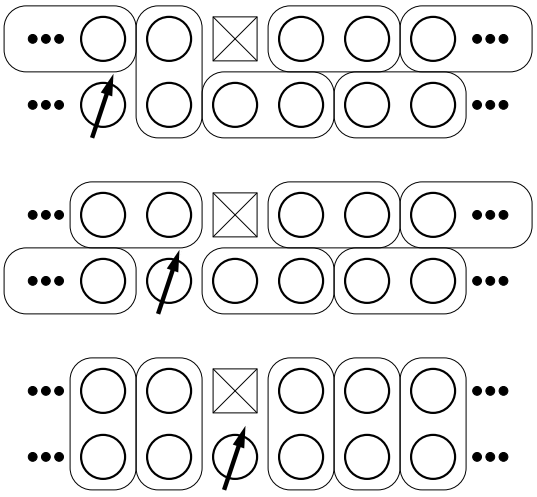

Figure 1.7: The resonating valence-bond (RVB) picture for the Heisenberg ladder with vacancy. One of the surrounding spins is clearly unpaired which has quite an impact on the microscopic properties of the material.

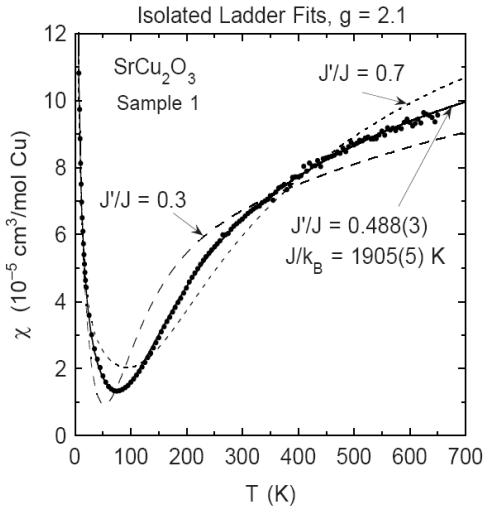

Figure 1.8: Different fits by Johnston et al. to experimental data using a model function (see eq. 1.5) for the susceptibility.

1.4 Theoretical Studies

1.4.1 DC. Johnston et al.: Magnetic Susceptibilities of Spin-1/2 Anti-Ferromagnetic Heisenberg Ladders and Applications to Ladder Oxide Compounds [1]

Johnston et al. carried out numerous QMC-simulations of the magnetic susceptibility of undoped $SrCu_2O_3$ and tried to fit them to experimental results. They basically fitted their simulations with the following model function:

$$\chi(T) = \chi_0 + \frac{C_{imp}}{T-\theta} + \chi^{spin}(T) \tag{1.5}$$

with

$$\chi_0 = \chi^{core} + \chi^{VV} \tag{1.6}$$

where χ^{core} is the orbital diamagnetic core contribution, χ^{VV} is the paramagnetic Van Vleck contribution (both are assumed to be temperature-independent), $C_{imp}/(T-\theta)$ is a Curie-Weiss term originating from impurities, and χ^{spin} is the intrinsic spin susceptibility. This leaves quite a few fitting parameters which makes accurate fittings even more difficult.

They also used different types of couplings additionally to the ones along the legs and rungs. E.g., they introduced a diagonal ferromagnetic coupling inside a plaquette of the

$J_\parallel/k_B$	$J_\perp/J_\parallel$	$J_{diag}/J_\parallel$	$J_{tr}/J_\parallel$	$J_3/J_\parallel$
1905(5)	0.488(3)			
1890(40)	0.482(13)	-0.10(5)		
2000(60)	0.465(13)		-0.1(1)	
1894(8)	0.5			0.009(4)

Table 1.1: Exchange constants for $SrCu_2O_3$ obtained by Johnston et al. [1] by fitting of susceptibilities χ for different models. J_{diag}: Intra-ladder diagonal, J_{tr}: Inter-ladder trellis, J_3: Inter-ladder stacked.

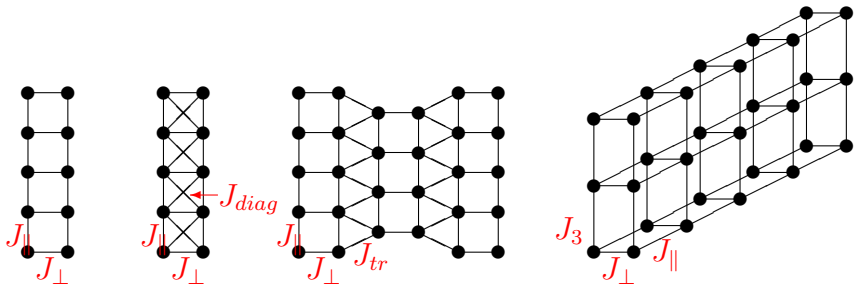

Figure 1.9: The different models used by Johnston at al. to fit susceptibility curves. See table 1.1 for results.

ladder which they found out not to exhibit any noticeable changes to the behavior of the spin system. Furthermore they assumed inter-ladder couplings both in the plane of the ladder and perpendicular to it. The coupling strengths they obtained are listed in table 1.1.

Johnston et al. also varied the Landé factor g but came to the conclusion that a value of about 2.1 is the correct one. For the anomaly of the non-isotropic coupling on the ladder itself, which cannot be described by the underlying chemistry of the C-O bonds, they call to account higher order exchange paths of the material. Furthermore they implied that the anisotropy of the bond strengths has its origin in the spatial asymmetry of the crystal. The lack of inclusion of the inter-ladder couplings in the ladder plane and perpendicular to it cannot be made responsible for the anisotropy in the material (see table 1.1).

Another possibility for a more accurate description is the introduction of a cyclic exchange term which depicts a hopping exchange in circles (see sec. 1.2.2). Johnston cites Mizuno, Tohyama and Maekawa [18] who found couplings including cyclic exchange of $J_\parallel/k_B = 2260(60)K, J_\perp/J_\parallel = 0.77(12), J_{diag}/J_\parallel = 0.015(10), J_{cycl}/J_\parallel = 0.092$.

1.4.2 Enhancement of Anti-ferromagnetic Correlations due to Vacancies

Laukamp et al. [19] observed an enhancement of real-space correlations near vacancies for Heisenberg chains as well as for ladder systems. They performed DMRG (see sec. 1.8) simulations for systems of size 32×2 and stated that this effect does not depend on the gapped or non-gapped characteristic. Furthermore they analysed the local susceptibility and found a staggered contribution in the vicinity of the vacancy.

1.4.3 Appearance of Effective Spin-1/2 Degrees of Freedom around Vacancies

Schollwöck et al. [13] have shown that an effective model using *unpaired spins* which are induced around vacancies on a spin-ladder can be used to successfully derive low-energy spectra using DMRG (see sec 1.8) methods. This model relies on the appearance of a spin-1/2 around such a distortion and on a secondary interaction between them. Additionally they described an anti-ferromagnetic component of the local magnetization on sites in an exponentially limited domain around the vacancy.

1.4.4 C. Calzado, C. de Graaf et al.: Four-spin Cyclic Exchange in Spin Ladder Cuprates [2]

Ab-initio calculations done by Calzado, de Graaf et al. support the idea of a necessary inclusion of a 4-spin-cyclic exchange term into the model (see sec. 1.2.2). They argue that an anisotropic spatial coupling on the ladders is not consistent with chemical and geometrical considerations of the material. Often inter-ladder interactions are made responsible for this but so far no further inclusion of these couplings indicated a reduction of the anisotropy. On the basis of quantum mechanical calculations they obtain a fraction of 30% coupling strength for a cyclic exchange.

1.5 Experimental Methods

1.5.1 Nuclear Magnetic Resonance (NMR)

Nuclear magnetic resonance (NMR) is a powerful non-destructive experimental method which relies on the existence of a core-spin in certain elements and allows direct visualization of the magnetic moment of the nucleus. Additionally due to the couplings with other spins it delivers insight in the whole spectrum of magnetic properties of a material [20].

In the nowadays widely confirmed standard model of elementary particle physics the proton as well as the neutron are associated with a spin of one half. This means that under some circumstances the spin of a core consisting of these particles can sum up to a finite value. As known from quantum mechanics this spin can orient differently with different energies to an external magnetic field in a quantized way. A conversion between these states can be induced by a second external high-frequency magnetic field. The observed quantity by stimulating either the primary constant magnetic field or the frequency of the secondary field is the absorption of the material.

Furthermore it can be imagined that the local spins of the electrons nearby the core alter the local magnetic field. The NMR resonance condition reads as follows [21]:

$$\nu_{RF} = \frac{\gamma}{2\pi}\left(H_0 + \left(\sum_i \hat{A}_{ij}\langle\vec{S}_i\rangle\right)^z\right) \tag{1.7}$$

where $\gamma/2\pi$ is the gyromagnetic ratio of the nucleus, H_0 is the static magnetic field, $\hat{A}$ is the hyperfine coupling tensor, $\vec{S}_i$ is the spin operator at the site i and ν_{RF} is the resonance frequency. $()^z$ denotes the z-component of a given vector.

Here it is sufficient to collapse the sum over several sites to one single site because the dominant coupling of the nuclear magnetic moment is certainly the one with the core's own electron's spin. The formula simplifies to:

$$\nu_{RF} = \frac{\gamma}{2\pi}\left(H_0 + A\langle S\rangle\right) \tag{1.8}$$

It is assumed that the local spin is proportional to the magnetic field:

$$\langle S\rangle(H_0) = \langle S\rangle(H_{\text{ref}})\frac{H_0}{H_{\text{ref}}} \tag{1.9}$$

where H_{ref} is a reference magnetic field. Inserting and rearranging of eq. 1.8 gives

$$H_0 = \frac{\nu_{RF}}{\frac{\gamma}{2\pi}}\frac{1}{1 + \frac{A}{H_{\text{ref}}}\langle S\rangle(H_{\text{ref}})} \tag{1.10}$$

So for constant resonance frequency this delivers a condition for each single electron magnetization, which adds up to the shape of the gained NMR-spectrum.

1.5.2 Neutron Scattering

Neutron Scattering became an important tool for examining magnetic properties of solid-state bodies. The neutron is a charge-less particle, which makes it ideal for non-destructive experiments, and it has spin, which allows direct interaction with the magnetic particles of the sample. Inelastic scattering allows to excite the specimen with spin-waves which are collective excitations in many materials. The most important physical quantity obtained is the spin-gap, which describes the energy of the lowest lying excitation compared to the ground state (see sec. 1.1.3).

1.6 Experiments

1.6.1 Fujiwara, Yasuoka: NMR Study of Zn Doping Effect in Spin Ladder System $SrCu_2O_3$ [3]

Samples of powdered $SrCu_2O_3$ were investigated by Fujiwara et al. by measuring nuclear magnetic resonance (NMR) spectra of ^{63}Cu and ^{65}Cu. They used specimens of the material doped with 0.25% and 0.5% Zn replacing the Cu atoms and carried out the NMR experiments at a frequency of 83.55 MHz.

They confirmed experiments done before with pure samples. The NMR spectrum has resonance peaks with a temperature-independent line-width of about 200G which can for the most part be identified with the minimum experimentally achievable width. On the other hand they observed a spectacular increase of the line-width with decreasing temperature for the doped samples (see fig. 1.10). The remarkable feature of Fujiwara's findings is the broadening not only for doping concentrations larger than 1% but for smaller concentrations, too. They tried to understand their experimental findings with a simple model consisting of an exponential decay of the local magnetic moments around the impurities $S_i^z = (-1)^i S_0 \exp(-i/\xi)$. Using this they came to the conclusion, that the correlation length ξ is of the order of 100 in the doped samples.

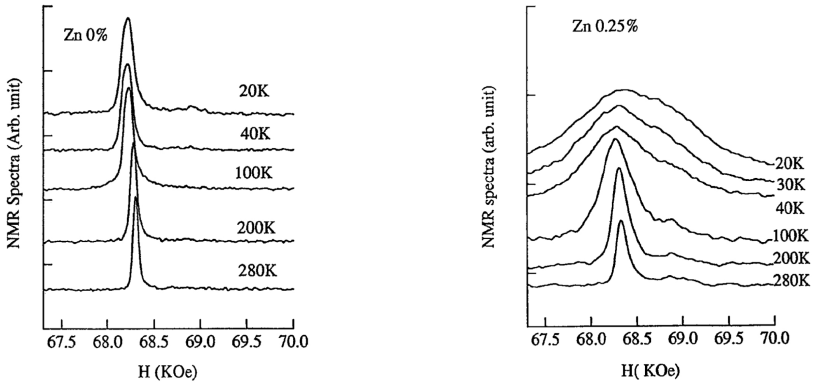

Figure 1.10: NMR spectra produced by Fujiwara et al. [3]. The ^{65}Cu central peak for the core-spin transition $-\frac{1}{2} \rightarrow +\frac{1}{2}$ at $\nu = 83.55$MHz is plotted for 0% and 0.25% doping density, respectively.

1.6.2 Oshugi et al.: Impurity Induced Staggered Polarization and Anti-Ferromagnet Order in Spin 1/2 Heisenberg Two-Leg Ladder Compound $SrCu_2O_3$: Extensive Cu NMR and NQR Studies [4]

It is reported that plotting the Neél-Temperature T_N of the material vs. doping concentration x leads to a broad maximum around $x = 0.04$. In the pure samples a spin-gap at $k = \pi$ is evident for even legged ladders while in the doped material a new excitation branch appears at zero energy.

The authors introduce a new picture called impurity-induced staggered polarization (IISP), which incorporates a correlation of these unpaired spins surrounding the dopants. They establish a second characteristic length, determining these correlations which appears to be much longer than the original correlation length according to the authors. Their fitting formula reads

$$S_l = (-1)^l S_0 \exp\left(-\frac{la}{\xi_s}\right) + (-1)^{L-l} S_0 \exp\left(-\frac{(L-l)a}{\xi_s}\right) \tag{1.11}$$

where l and $L - l$ denote the distances from the impurities. The used as S_0 a value of $\frac{1}{2}$ which emphasizes the fact, that they describe a correlation *between* the induced spin-1/2.

The enhancement of AF correlations near vacancies have been the focus of Laukamp et al. [19].

In their NMR experiments Oshugi et al. also saw the line-width-broadening at lower temperatures. They could reduce this phenomenon to the following formula

$$\Delta H = \frac{W}{T} + \Delta H_c$$

where ΔH is the line-width, W and ΔH_c are constants.
However, in their simulations they used an uniform distribution of dopants on the ladder. In conclusion they present a formula connecting the correlation length and the vacancy distribution:

$$\xi = A + BD_{AV}$$

where ξ is the correlation length, A and B are constants, and D_{AV} is the mean distance between vacancies.

1.6.3 M. Azuma and M. Takano: Disappearance of the Spin-Gap in a Zn Doped 2-Leg Ladder Compound $Sr(Cu_{1-x}Zn_x)_2O_3$ [5]

Azuma and Takano performed a series of inelastic neutron scattering studies on $SrCu_2O_3$ with impurity concentrations $x = 0$, $x = 0.003$, $x = 0.006$, $x = 0.01$, $x = 0.02$, and $x = 0.04$. They confirmed the widely believed spin-gap of about $400K$ [22, 23, 24] not only for the undoped material but also for the samples with impurities. Furthermore they discovered that the integrated intensity of the neutron scattering just above the spin-gap energy decreases towards a concentration of $x = 0.04$, where it vanishes. This intensity corresponds to the gapped singlet-triplet excitation.

1.6.4 M. Azuma et al.: Switching of the Gapped Single Spin-Liquid State to an Anti-Ferromagnetically Ordered State in $Sr(Cu_{1-x}Zn_x)_2O_3$ [6]

A series of experiments was done by M. Azuma et al. by measuring specific heat and magnetic susceptibility for $SrCu_2O_3$ with impurity content of up to 8%. They referred to the resonating valence-bond (RVB) picture (see sec. 1.3) and confirmed the inducing of spin-1/2 near the dopants on the ladder in the low impurity limit. They found evidence for an onset of magnetic ordering for doping densities starting from $x = 0.01$ by observing anomalous cusps in specific heat and susceptibility vs. temperature plots

peaking at $x = 0.04$. For higher concentrations the correlations decrease due to break-ups by the impurities.

1.7 Monte Carlo

Monte Carlo methods (MC) [25] are powerful tools to examine solid state bodies. As a numerical method they simulate e.g. the magnetic behavior of materials. Many different kinds of MC have been developed. In Quantum Monte Carlo the representation in SSE (Stochastic Series Expansion, see sec. 1.7.3) has been very successful. This section can only be seen as a short introduction into the large topic of Monte Carlo and its different types.
In principle Monte Carlo methods approximate the partition function and thermodynamical averages of other physical observables. The simple form of the average is

$$\langle \hat{O} \rangle = \frac{\sum_\phi \langle \phi | \hat{O} \exp\left(-\beta \hat{H}\right) | \phi \rangle}{\sum_\phi \langle \phi | \exp\left(-\beta \hat{H}\right) | \phi \rangle} \tag{1.12}$$

where $\hat{O}$ denotes any observable and $\exp\left(-\beta \hat{H}\right)$ is the usual Boltzmann weight with the Hamilton operator $\hat{H}$ and the inverse temperature β. The sum spans over all possible states $|\phi\rangle$ of the Hilbert space. Treating this sum directly in a numerical way is quite unpractical because it would produce a necessary effort far too much for present computers. Therefore the sum has to be replaced by

$$\langle \hat{O} \rangle \approx \frac{1}{N} \sum_{i=1}^{N} O[\phi_i] \tag{1.13}$$

which sums measurements $O[\phi_i]$ over states out of a Markov chain produced by a suitable Monte Carlo algorithm. These states are sampled according to the probability distributions in equation 1.12 and give an estimator for the thermal average of the observable for large enough N. Because Markov chains are a succession of configurations correlated with each other, sophisticated error checks have to be made. The number describing the amount of correlation is called the *auto-correlation time*.
Two major requirements have to be fulfilled for every Monte Carlo algorithm:

- *Ergodicity* makes sure that every possible state in the Hilbert space can be reached in finite time. Ensuring this is not always a trivial task, even in simple systems.

- *Stationarity* provides for the correct probability distribution of the obtained states. It essentially says that a correct distribution is a fixed point of the Monte Carlo update.

1.7.1 The Sign Problem

The sign-problem is caused by the appearance of negative weights for some Monte Carlo configurations under special circumstances. For Heisenberg models this applies to geometrically frustrated lattices with anti-ferromagnetic coupling. In principle, such systems are treatable with Monte Carlo algorithms but they become exponentially slow which essentially makes usage impossible in many cases.

1.7.2 Error Management in Monte Carlo

Assuming independent values in eq. 1.13 the statistical error is: [26]

$$\Delta O = \sqrt{\frac{\sigma_O^2}{N}} \qquad \text{with} \quad \sigma_O^2 = \langle O^2 \rangle - \langle O \rangle^2 \tag{1.14}$$

As stated above the values O_i are *not* independent, which makes it necessary to apply a correction:

$$\Delta O = \sqrt{\frac{\sigma_O^2}{N} 2\tau_{int}} \tag{1.15}$$

where τ_{int} is the integrated correlation time which is a measure of correlations of consecutive observable values in the Markov chain.
Further sophisticated methods of analyzing existing Markov chains after performing the simulation are:

- *Binning* segments the chain into smaller blocks which are examined separately. The amount of values per block is increased continuously and the variance of the means of each block is calculated. It can be shown that it converges to the exact value of the error, when the range of a single block exceeds the correlation time.

- *Jackknife* partitions the chain into blocks of fixed length and then calculates the variance of means of the chain N_B times, each time leaving out one block. The total variance is the mean of this values multiplied by a factor $N_B - 1$.

1.7.3 The SSE Representation

The treatment of quantum mechanical systems with Monte Carlo algorithms is realized by the use of an additional dimension in order to project it onto a classical system. There are different ways of doing so, a fairly simple method used here is the *stochastic series expansion (SSE)* [27].
Its foundation is an expansion of the partition function.

$$
\begin{aligned}
Z = \mathrm{tr}\left(\exp\left(-\beta H\right)\right) &= \sum_{n=0}^{\infty} \frac{\beta^n}{n!} \mathrm{tr}\left(-H\right)^n && (1.16)\\
&= \sum_{n=0}^{\infty} \frac{\beta^n}{n!} \sum_{\phi_1 \ldots \phi_n} \sum_{b_1 \ldots b_n} \langle\phi_1| - h_{b_1} |\phi_2\rangle \langle\phi_2| - h_{b_2} |\phi_3\rangle \ldots \langle\phi_n| - h_{b_n} |\phi_1\rangle \\
&= \sum_{n=0}^{\infty} \frac{\beta^n}{n!} \sum_{\phi_1 \ldots \phi_n} \sum_{b_1 \ldots b_n} \prod_{i=1}^{n} \langle\phi_i| - h_{b_i} |\phi_{i+1}\rangle && (1.17)
\end{aligned}
$$

In the second line the Hamiltonian $H = \sum H_{b_i}$ was decomposed into parts H_{b_i} which act on specific bonds b_i of the system. It is easy to understand that the Heisenberg model's bond terms are indeed in this form, whereas the site terms can be transformed to bond terms distributing their action on a specific site to neighbouring bonds. The state of the system as well as the operators are usually written in the S_z-eigenbasis.
Writing the partition function in this form enables us to formulate a scheme similar to world lines in continuous imaginary time [26]. The major difference is that in SSE there is a discrete index $i = 1 \ldots n$ compared to the continuous time in the world-line representations.
A composition of states ϕ_i and operators H_{b_i} is denoted as an elementary configuration of the algorithm. For a one-dimensional system these configurations can be pictured as a bunch of lines on a rectangular lattice, where one direction denotes the site index and the other the SSE-index (see fig. 1.11). Two different site states are then represented as existence or absence of the line at the specific site. These lines are able to hop from one site to a neighbouring one which occurs at SSE-indices where non-diagonal operators exist. A possible *local* update scheme is the alteration of the world line at specific points on the described plane.
Monte Carlo simulations are used to update the operators and sites as well as the expansion order n. This allows to treat the *exact* Hamiltonian in the simulation, no other approximations than those of the Monte Carlo method are used.

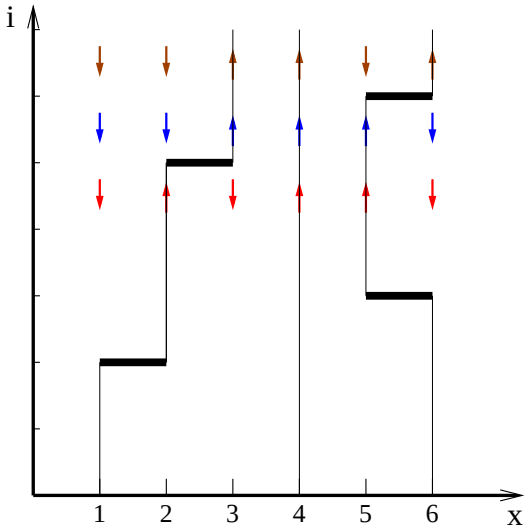

Figure 1.11: The SSE representation. In the upper part the corresponding spin configurations are depicted additionally.

1.7.4 The Loop Algorithm in SSE Representation

Local updates of the SSE configurations described above suffer from critical slowing down at second order phase transitions. Furthermore updates of some observables like the winding number which is used to measure the spin-stiffness have an exponentially small acceptance rate [28].

In the loop operator representation loop lines are introduced, which run along SSE-index direction and represent the actual spin state up or down by their direction they have at a particular site. It can be shown [26] that all possible hoppings of one site to another in the world-line picture (see fig. 1.11) can be represented as a single *horizontal break-up* operator in the loop representation. These operators then define the shape of the loops by acting as guides for building them (see fig. 1.12).

These operators can simply be inserted on the plaquettes of the checkerboard-like lattice with rather simple Metropolis probabilities. Consecutively a new configuration of loops is built fitting to the spin configuration at the bottom of the lattice. Now an actual update may be performed on the built loops, which means changing their direction and therefore reverting the spins. Afterwards the whole process can be repeated by starting to update the operators again.

The actual implementation of this algorithm is a little different. First of all a maximal string length is introduced, which allows for the limitations in computational simulations.

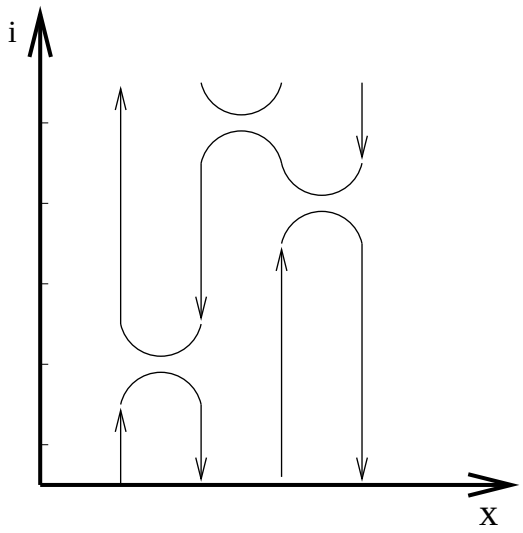

Figure 1.12: The Loop Algorithm in SSE representation.

The so-called *operator string* has therefore a fixed size and the change of expansion order is realized by insertion or taking out of unit operators. Furthermore the loops are realized by double-linked lists, which allows easy handling with the loops.

1.7.5 The Directed Loop Algorithm

The directed loop algorithm alters mainly the way the loops are built compared to the loop algorithm described above. Additionally it allows the loop to self-intersect and backtrack [29]. Similar to the Worm algorithm it starts at a source term which is either a creation (S^+) or annihilation (S^-) operator and crawls its way through the configuration until it reaches the mentioned source term again. The direction it takes is decided locally at each plaquette, according to probabilistic rules ensuring detailed balance. The spins are reverted immediately during the process of construction. It suffices to build only one loop and then start with the operator update again.
The advantages are the possibility of efficiently handling a more general class of Hamiltonians including ones with extensive magnetic fields.

1.7.6 The ALPS Library

The ALPS project (algorithms and libraries for physics simulations) [30] is building collection of open source libraries and applications. Its goal is to provide a standardized

pool of such programs for all sectors of physics and related sciences.
In the course of this diploma thesis code from this project has been used and many alterations to it have been made.

1.7.7 Modifications to the ALPS Program

Alterations to the ALPS library: A handling for multiple vacancies was added in a rather primitive but effective way. The couplings of the vacant site as well as the local magnetic field were simply set to zero.

Alterations to the ALPS applications: Several Observables have been added to the implementation of the QMC program in SSE representation. These are e.g. the staggered structure factor, the staggered susceptibility, and the staggered local magnetization for each site, which has been implemented not only for one time slice but as an average over the whole SSE representation string. Furthermore a class for measuring the imaginary time correlations has been added by using proper observable definitions from the ALPS library in order to be able to compute errors for all observables as well. This has been done to measure correlations mainly in momentum space, but for some tests also a method for real space correlations was implemented. A proper treatment of the winding number in each dimension, which delivers an improved estimator for the spin stiffness was added, too.

Additions to the model and lattice library: Additional lattice types were programmed for trellis lattices, stacked lattices and additional model Hamiltonians were built for vacancy treatment and spatial diagonal terms.

1.7.8 Spin-Gap and Correlations

1.7.8.1 Correlations in SSE

In order to obtain the imaginary time correlations a conversion from the discrete SSE index to imaginary time has to be made [31]. This is done the following way.
For each SSE index consecutive numbers between 0 and β are cast and compared to a given set of equally distributed imaginary times in the same interval. This allows to find a spin configuration for each of these time slices.

The Green's functions obtained this way can be used to plot an excitation spectrum of the system using the maximum entropy algorithm (see sec. 1.10).

1.7.8.2 Imaginary Correlation Length and Spin-Gap

The spectral theorem states [32]:

$$G_\tau = \int_{-\infty}^{\infty} \frac{A(\omega)\exp(-\omega\tau)}{\exp(-\beta\omega)+1} d\omega \tag{1.18}$$

where $A(\omega)$ is the spectral function. Introducing the *dynamical structure factor* $S(\omega) = A(\omega)/(1+\exp(-\beta\omega))$ leads to

$$G_\tau = \int_{-\infty}^{\infty} S(\omega)\exp(-\omega\tau)\, d\omega \tag{1.19}$$

Moreover assuming that there is no excitation below a specific energy value (the spin-gap) and that the edge of the domain with excitation can be expressed as a Dirac-δ-functional gives

$$G_\tau = \int_{-\infty}^{\infty} \delta(\omega-\omega_0)\exp(-\omega\tau)\, d\omega = \exp(-\omega_0\tau) \tag{1.20}$$

The Green's function decays in an exponential way. Therefore the excitations with larger energies than the actual spin-gap deliver faster decaying modes of the imaginary time correlation function. The result

$$\omega_0 \cong \frac{1}{\xi_\tau} \tag{1.21}$$

states that the spin-gap is the inverse of the correlation length in imaginary time direction.

1.7.8.3 The Dynamical Critical Exponent

In addition to the critical exponents stated in sec. 1.1.6 the *dynamical critical exponent* is defined as follows.

$$\xi \propto \xi_\tau^z \tag{1.22}$$

where ξ is the (spatial) correlation length, ξ_τ is the correlation length in imaginary time direction, and z is the dynamical critical exponent. Like the other critical exponents it describes the limit behaviour at a phase transition and it expresses the proportionality of the two characteristic lengths.

1.7.9 Finite Size Scaling (FSS)

An important tool to analyse data of critical phenomena obtained by numerical simulations is *finite size scaling (FSS)* [14]. It relies on the theory of critical exponents (see sec. 1.1.6) and on the assumption that the properties determined by the size of the system are functions of the ratio L/ξ alone. Here, L is the linear size of the system and ξ is the correlation length.
Bearing this in mind one can write:

$$A(L, j) = j^{-\gamma} f_1 \left(\frac{L}{\xi} \right) \tag{1.23}$$

where A is a measured observable, j is a parameter (e.g. a reduced coupling strength which vanishes at the critical point i.e. $j = (J - J^{crit})/J^{crit}$) and γ is some critical exponent. Using $\xi = j^{\nu}$ and multiplying the equation by $L^{-\frac{\gamma}{\nu}}$ leads to:

$$L^{-\frac{\gamma}{\nu}} A(L, j) = (L^{\frac{1}{\nu}} j)^{-\gamma} f_2 \left(L^{\frac{1}{\nu}} j \right) = f_3 \left(L^{\frac{1}{\nu}} j \right) \tag{1.24}$$

f_1, f_2 and f_3 are any functions. Plotting $L^{-\frac{\gamma}{\nu}} A(L, j)$ over $L^{\frac{1}{\nu}} j$ for different values of L *and* j results for correct critical exponents in a single curve. This can be used to determine the critical exponents themselves by altering them successively.

1.8 The Density Matrix Renormalization Group (DMRG)

The main advantages of the density matrix renormalization group method [33] are the absence of the negative sign problem and the possibility of examining fairly large systems with high precision at zero temperature. Some tricks make it even possible to find the first excited states in addition to the ground state. Disadvantages are mainly the strong dimensional limitations as well as the treatment of periodic boundary conditions (pbc), which is much slower than using open boundary conditions due to the density matrix representation [34].
The DMRG method relies on a consecutive build-up of a wave function in a reduced Hilbert-space which is created by alternatingly building tensor products of quantum mechanical states and truncating the amount of states kept.
The usage of the so-called real-space renormalization group, which discards all states but the ones with the lowest energies, leads to problems. It assumes that the ground state

Figure 1.13: The DMRG method. There is a system block to the right and an environment block to the left. The two sites in the center are added at a particular step.

of a combined system can be produced as a linear combination of the lowest eigenstates of the smaller systems. That this can't reproduce a variety of systems can be seen by considering the primitive particle in a box model. Combining two of these boxes to one large box leads to a problem in the center of the new box because all eigenstates of the smaller boxes vanish there and no finite value for the wave function can be constructed which certainly would have to be done for the new ground state.

The way out is using a so-called environment block which mimics the surroundings of the actual system. So the outline of the whole process is that starting form a Block S with size l it is expanded by a new site to size $l+1$. Furthermore an environment block with the same size together with the expanding site is used to simulate the surroundings (see fig. 1.13).

The next step after adding the site is to truncate the Hilbert-space in order to remain able to calculate with reasonable numerical effort. The utilisation of density matrices allows to take the states with the largest weights in the density matrix eigenbasis. This does not only reduce the error for expectation values of arbitrary operators but it also optimizes the remaining wave function.

1.8.1 Finite-System DMRG

In order to simulate a finite system the system block is increased at the cost of the environment block after it has reached the desired size. Afterwards the direction of growing is changed and the former environment block is increased at the cost of the former system block (see fig. 1.14). This can be repeated several times to achieve better results. These considerations show that periodic boundary conditions are indeed a problem for DMRG because some sites of the system always remain unique.

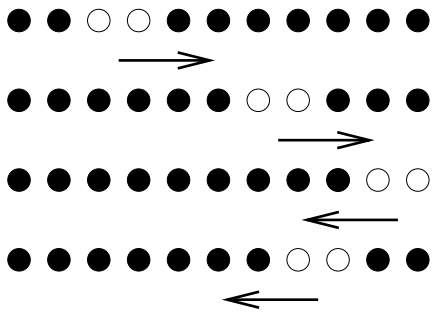

Figure 1.14: Finite system DMRG. The system block is increased at the cost of the environment block. After reaching the boundary the roles are switched.

1.8.2 DMRG Program by Noack and White

The DMRG program used in this thesis was designed by Reinhard M. Noack, Steven R. White and Eric Jeckelmann, although it was altered consecutively by several users. It was written in C++ and relies on a object oriented programming style.

1.8.3 Alterations to the DMRG Program

The trellis lattice type was added to the program as well as a proper handling of vacancies. Furthermore additional terms for the Hamiltonian were added for the diagonal terms on the plaquettes and for the cyclic exchange term.

1.9 The NMR Program

The program for simulations of nuclear magnetic resonance (see sec. 1.5.1) experiments was built from scratch in C++ in an object oriented style. This leads to efficient using of e.g. magnetic profiles which can be merged, added and generally dealt with in a self-explaining way. The program is able to distribute vacancies with specified probability in an arbitrary way on a given system and calculates magnetic profiles either accordingly to a given data set of magnetic behavior near a vacancy or using a simple exponential decay. Furthermore it is possible to input entire collections of magnetic profiles of nearby vacancies, which are used to reproduce effects which might occur due to neighbouring vacancies. Also a fairly simple Monte Carlo algorithm to pay tribute to possible different weights of configurations was implemented.

Eq. 1.10 delivers the following method for sampling using the expression:

$$\frac{\nu_{RF}}{\frac{\gamma}{2\pi}} \frac{1}{1 + \frac{A}{H_{ref}} S_m(H_{ref})} \tag{1.25}$$

for many characteristic spin values S_m, distributed as in the material itself. This can be plotted as a histogram. To simulate real world experiments an additional line-width is added to smear out the resulting resonance peaks.

1.9.1 Parameters

For the simulations in this thesis the following parameters according to the experiments by Fujiwara et al. [3] have been used:

- $A = -120\text{kOe}/\mu_B \equiv -12\text{T}/\mu_B$
- $H_{ref} = 23.824\text{T} \equiv 0.01 J_{\parallel}$
- $\gamma/(2\pi) = 12.0985\text{MHz/T}$
- $\nu_{RF} = 83.55\text{MHz}$

1.10 Maximum Entropy Program

The maximum entropy algorithm [35] was used to reconstruct the spectral function $A(\omega)$ from given greens functions and relation 1.18:

$$G(\tau) = \int_0^\infty S(\omega) \exp\left(-\omega\tau\right) d\omega \tag{1.26}$$

where $S(\omega) = A(\omega)/(1 + \exp\left(-\beta\omega\right))$ is the dynamic structure factor [36]. This is essentially an inverse Laplace transformation. The method relies on applying theory of probabilities onto this equation. The Bayes theorem states:

$$p(S(\omega)|G(\tau), \mathcal{B}) = \frac{1}{Z} p(G(\tau)|S(\omega), \mathcal{B}) p(S(\omega)|\mathcal{B}) \tag{1.27}$$

The Prior $p(S(\omega)|\mathcal{B})$ is essentially a Poisson distribution, assuming that after discretising the $S(\omega)$ the addition of a quantum ΔS is independent of already added values:

$$P(\vec{n}|\vec{\mu}, \mathcal{B}) = \exp\left(-\sum_i \mu_i\right) \prod_{i=1}^{N} \frac{\mu_i^{n_i}}{n_i!} \tag{1.28}$$

where n_i is a discrete index for the $S(\omega)$ ($S(\omega_i) = n_i \Delta S$) and the μ_i are expectation values. Applying Stirling's formula:

$$P(\vec{n}|\vec{\mu}, \mathcal{B}) = \frac{1}{Z} \frac{1}{\prod_i \sqrt{n_i}} \exp\left(\sum_i (n_i - \mu_i - n_i \log(n_i/\mu_i) \right) \tag{1.29}$$

This leads to a generalization of the Shannon-entropy:

$$\mathcal{S} = \sum_{i=1}^{N} n_i - \mu_i - n_i \log(n_i/\mu_i) \tag{1.30}$$

Defining $\alpha \equiv 1/\Delta S$ and rediscretising one obtains:

$$P(S(\omega_i), \mathcal{B}) = \frac{1}{Z(\alpha)} \frac{1}{\prod_i \sqrt{S(\omega_i)}} \exp\left(\alpha \sum_i (S(\omega_i) - m_i - S(\omega_i) \log(S(\omega_i)/m_i)) \right) \tag{1.31}$$

where $m_i = \mu_i \Delta S$.
For calculation of the norm a steepest descent approximation has to be used, assuming that the entropy is dominated by a small peak. Generally the steepest descent approximation reads:

$$\int_0^\infty \exp(f(x))\, g(x) dx \approx (2\pi)^{\frac{N}{2}} g(x^*) \exp(f(x^*)) \frac{1}{\sqrt{\det\left(-\frac{\partial^2}{\partial x_i \partial x_j} f(x) \Big|_{x^*} \right)}} \tag{1.32}$$

where $\exp(f(x))$ is peaked around x^* and $-\frac{\partial^2}{\partial x_i \partial x_j} f(x)$ is the Hessian. Applying this one easily calculates for the prior:

$$P(S(\omega_i), \mathcal{B}) = (2\pi)^{-\frac{N}{2}} \alpha^{\frac{N}{2}} \frac{1}{\prod_i \sqrt{S(\omega_i)}} \exp\left(\alpha \sum_i (S(\omega_i) - m_i - S(\omega_i) \log(S(\omega_i)/m_i)) \right) \tag{1.33}$$

The likelihood $P(G(\tau)|S(\omega)\mathcal{B})$ is calculated by assuming an additive noise and therefore is a multivariate normal distribution:

$$P(G(\tau)|S(\omega)\mathcal{B}) \propto |C|^{-1/2} \exp\left(-1/2 \sum_{i,j} \Delta S(\omega_i) \left(C^{-1}\right)_{ij} \Delta S(\omega_j) \right) \tag{1.34}$$

where $\Delta S(\omega_i)$ is the difference to the theoretical value of $S(\omega_i)$. The posterior probability is then finally

$$P(S(\omega)|G(\tau)\mathcal{B}) = \frac{1}{Z} \exp\left(-\frac{1}{2}\chi^2 + \alpha S \right) \tag{1.35}$$

where χ^2 is the miss-fit, the quadratic form in the exponent of eq. 1.34.
The program used in this thesis was implemented by Wolfgang von der Linden and advanced by Danilo Neuber and Martin Hohenadler.

2 Results: Single Ladder

It has been shown by Johnston et al. (see sec. 1.4.1) that the dominating couplings in the material $SrCu_2O_3$ are along the legs and rungs of the ladders which emerge from the crystallization (see sec. 1.1.4). In this chapter magnetization profiles, NMR spectra, excitation spectra and correlation plots will demonstrate the effects of the insertion of vacancies on the ladder. Further considerations will include interactions beyond the simple ladder, e.g. diagonal and cyclic couplings. Also a spin-anisotropy will be introduced to the Heisenberg model.

2.1 The Isotropic Ladder

First of all the isotropic ladder was examined by DMRG methods. The term isotropic refers in this case to equal coupling strengths in different spatial directions.
A first plot is presented in fig. 2.1. The system size is 40 in x- and 2 in y-direction, no magnetic field was implemented, and the overall magnetization was set to zero. Due to symmetry considerations one clearly sees that all magnetic moments of each site have to vanish. Furthermore the plot shows correlations from a point $(19, 0)$, which evidently show staggered exponential decay. An estimate for the correlation length of the isotropic ladder is $\xi = 3.1(2)$. Note: indexing in every direction is always starting from 0, see fig. 2.2 for convention.
Applying a small magnetic field would lead to a constant magnetic moment for all spins. This is mimicked in fig. 2.3 by setting the target magnetization to 1. In this figure one can notice the imperfect convergence (pbc, see sec. 1.8). Although the states kept have been increased to 300 one clearly sees in the graph for the local magnetic moments that the sites are not equal.
Obviously, the insertion of a vacancy into the ladder removes the spatial symmetry of the system. In figures 2.4 and 2.5 one can see how the magnetization profile reacts to the vacancy. Notably a total spin-1/2 for the magnetization was required by the DMRG program because of an odd amount of spins. This total spin-1/2 is distributed around

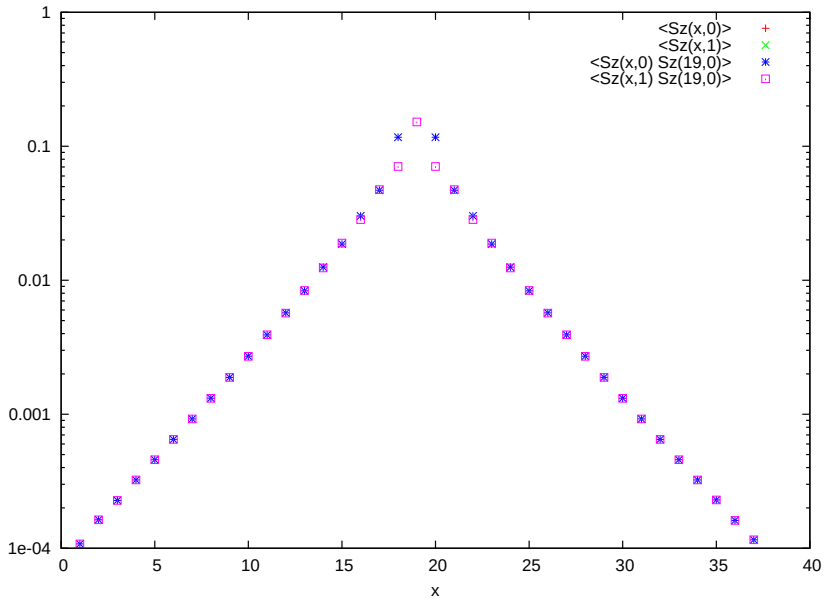

Figure 2.1: Staggered correlations and absolute magnetizations of an isotropic 40×2 ladder system for each site. Correlations were measured from site $(19, 0)$.

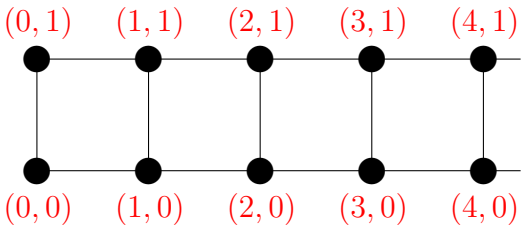

Figure 2.2: Indexing convention for ladders.

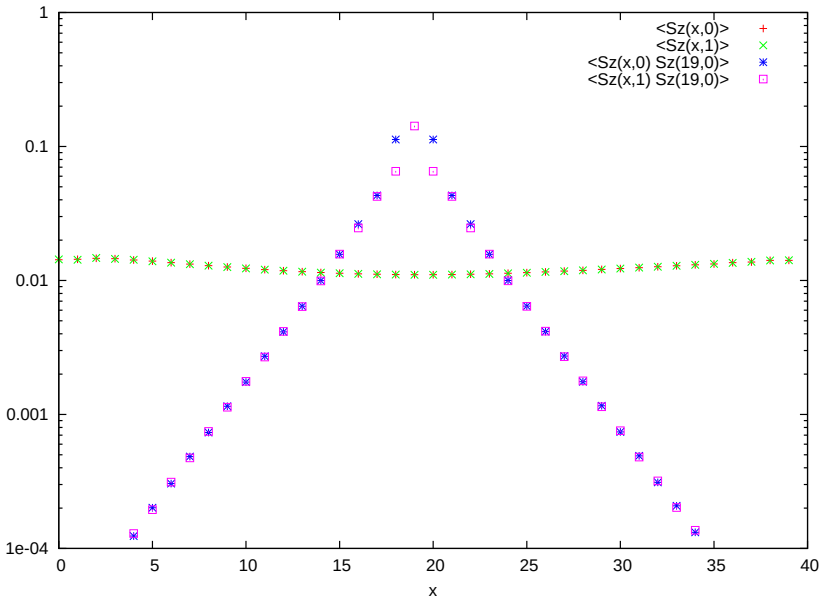

Figure 2.3: Correlations and magnetizations of an isotropic 40×2 ladder system for each site with overall magnetization 1 and periodic boundary conditions. Correlations were measured from site $(19, 0)$.

the vacancy, as one can see in the figures. This can be understood by remembering the resonating valence-bond picture of sec. 1.3. The single unpaired spin introduced there is reflected in this *spin-cloud* around the vacancy. Furthermore the exponentially decreasing magnetic moment of the spins with alternating sign is evident. Here, periodic boundary conditions were applied, too.

A typical plot for the appearance of 2 vacancies is given in fig. 2.6. This plot also shows the same decrease of correlations and magnetic moments as fig. 2.1.

2.2 The Anisotropic Ladder

2.2.1 DMRG

In contrast to the examples above it is widely believed that the material $SrCu_2O_3$ is best approximated by a ladder with different coupling strengths along and perpendicular to the major ladder axis. Many sources predict a ratio of $J_\perp/J_\parallel = 0.5$ [1]. Figure 2.7 is a plot of the same system as in fig. 2.6, revealing that the increasing coupling strength along the chain increases the correlation length and boosts the chain characteristics of

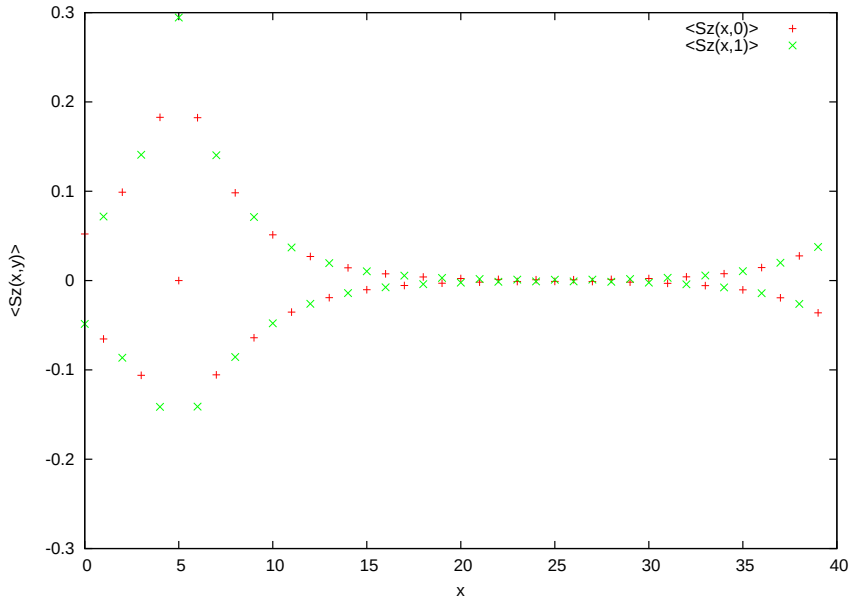

Figure 2.4: Magnetizations of an isotropic 40×2 ladder system with vacancy at $(5, 0)$ and periodic boundary conditions, plotted with linear scale.

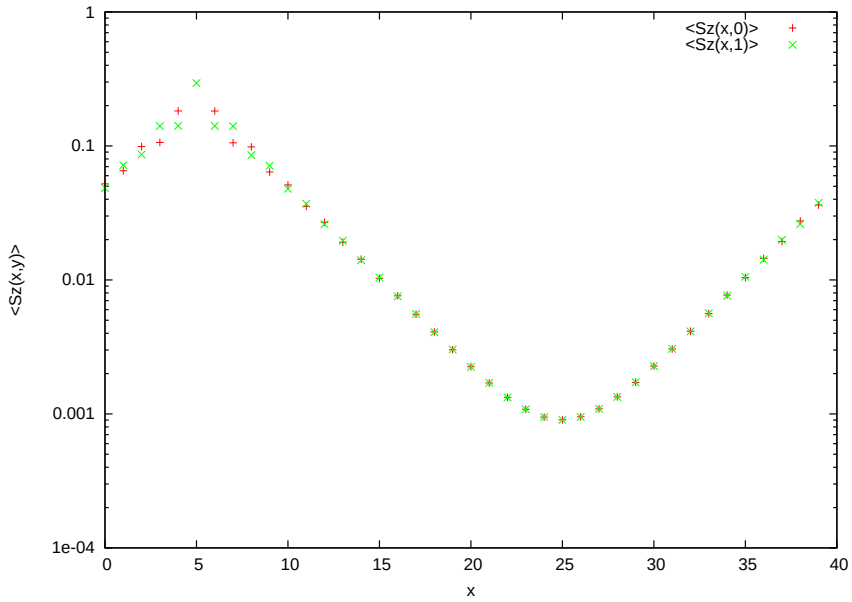

Figure 2.5: Absolute magnetizations of an isotropic 40×2 ladder system with vacancy at $(5, 0)$ and periodic boundary conditions, plotted with logarithmic scale.

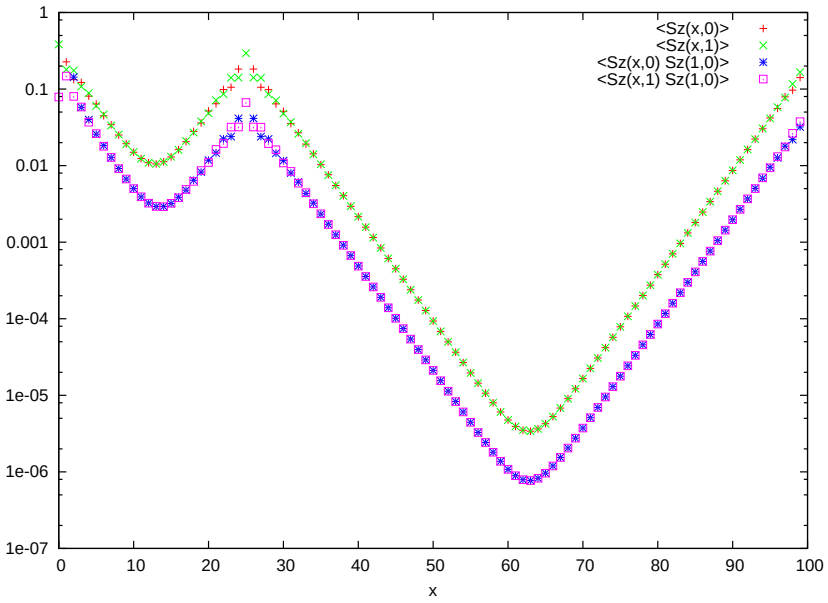

Figure 2.6: 2 Vacancies at sites $(0,0)$ and $(24,0)$ on the 100×2 isotropic ladder (pbc).

the system. As stated in sec. 1.1.2, the chain exhibits critical behavior which corresponds to an infinite correlation length.
The correlation length increases to $\xi = 7.2(2)$.

2.2.2 QMC

To produce similar plots with the QMC program in SSE representation an adaptation had to be made. In order to calculate the magnetic moments of the individual sites with a justifiable error margin an approach different to that one already implemented in the used program had to be adopted. Whereas for the summation of spins (e.g. for magnetization and structure factor) considerations of not only one time slice at $\tau = 0$ are redundant, for the individual spin it is necessary to get a reasonable error. Therefore means of the local moments over all times are used. Fig. 2.8 shows a magnetization profile similar the the ones obtained by DMRG. Here, an additional magnetic field $h = 0.01$ was applied.

2.2.3 NMR-Spectra

NMR experiments are used in solid state physics to examine magnetic properties of materials (see sec. 1.5.1). Simulations of such procedures and comparisons with the real

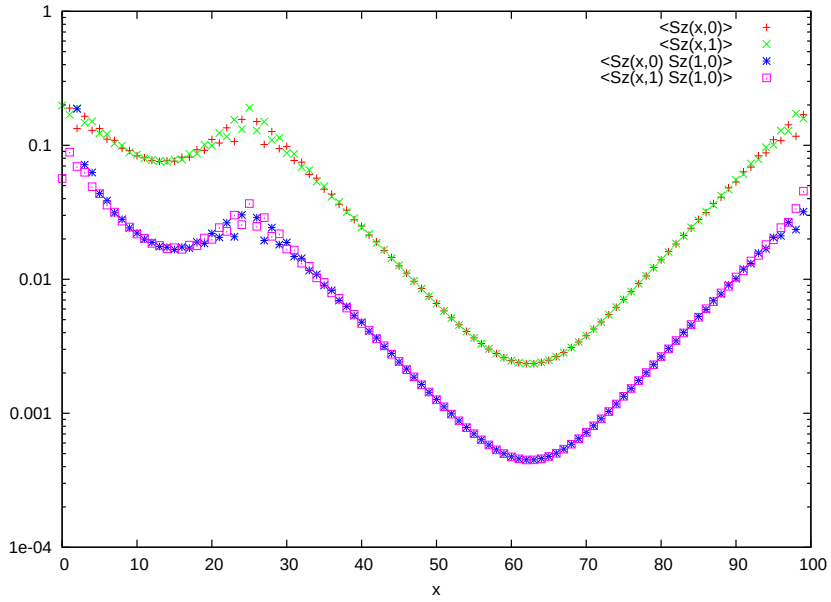

Figure 2.7: 2 Vacancies at $(0,0)$ and $(24,0)$ on the 100×2 ladder. (pbc)

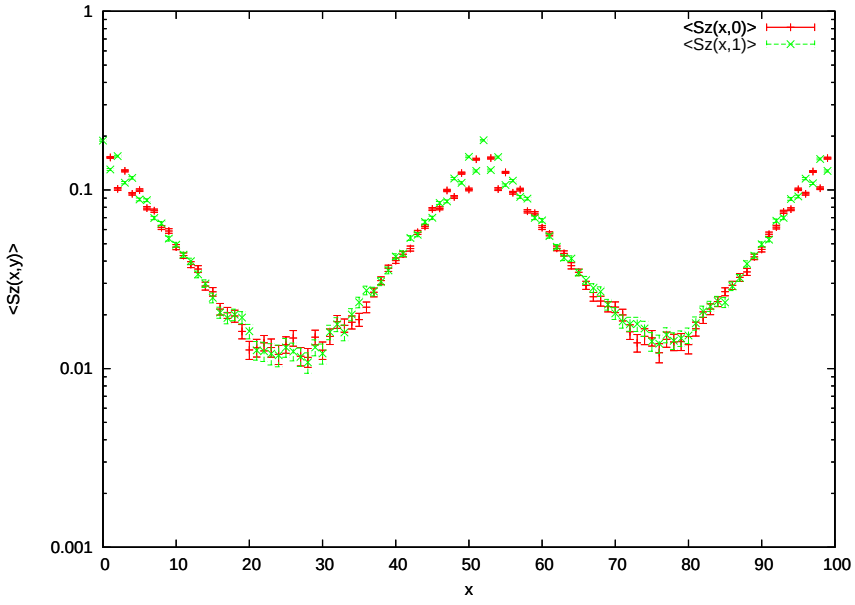

Figure 2.8: 2 Vacancies at $(0,0)$ and $(52,0)$ on the 100×2 ladder, obtained by QMC. (500000 steps)

experiment could lead to confirmation or decline of a theoretical model.
One has to either simulate the magnetization profiles or calculate them by assuming a theoretical characteristic. These magnetization values of the individual sites have then to fulfil the resonance condition 1.25 separately. A NMR spectrum can be drawn by plotting the relative frequency of resonance for each specific magnetic field strength.
The simplest way to get the needed distribution of magnetization values is to assume a staggered exponential decay using only two parameters, the correlation length and an absolute value of the magnetization next to the vacancy. To mimic real solid-state bodies it is necessary to sum over many configurations of vacancies on a given system and use the above data to calculate magnetization profiles for each of them.
The NMR spectra produced can be seen in figures 2.9 and 2.10. The first plot shows the direct output from the NMR program. The distinct resonance peaks around the main peak reflect clearly the discrete amounts of magnetic moments which appear in the material around the vacancy. The main peak itself results from the many sites which are not primarily influenced and have a magnetic moment close to zero. The second figure shows setup but with an additional Gaussian smearing which should reflect the actual shape of an experimentally achieved picture. The main reason for the broadening is the natural line-width and experimental imprecision.
Alternatively magnetic profiles can be taken directly from the QMC or DMRG simulations which should give a more accurate description of the magnetic conditions around vacancies. To reproduce many different vacancy configurations the program is able to use the single-vacancy profile, reproduce it for each vacancy location, and add them all up to arrive at a proper magnetic profile for the actual configuration.
Additionally another approach was used. In order to avoid the massive fluctuations of the profiles obtained by QMC far away from the vacancies but on the other hand in order not to have to abandon the unique magnetic structure around the vacancies, a domain around the vacancy was taken directly from the simulation whereas the other values were approximated by a simple exponential decrease (see fig. 2.11).
The resulting NMR spectra are shown in fig. 2.12 which leads to the conclusion that actually the different approaches don't lead to different results.

2.2.4 Vacancy Configuration Weights

The system may favour the positioning of vacancies at small distances, so some configurations would have to be sampled with larger weights. To examine the influence on

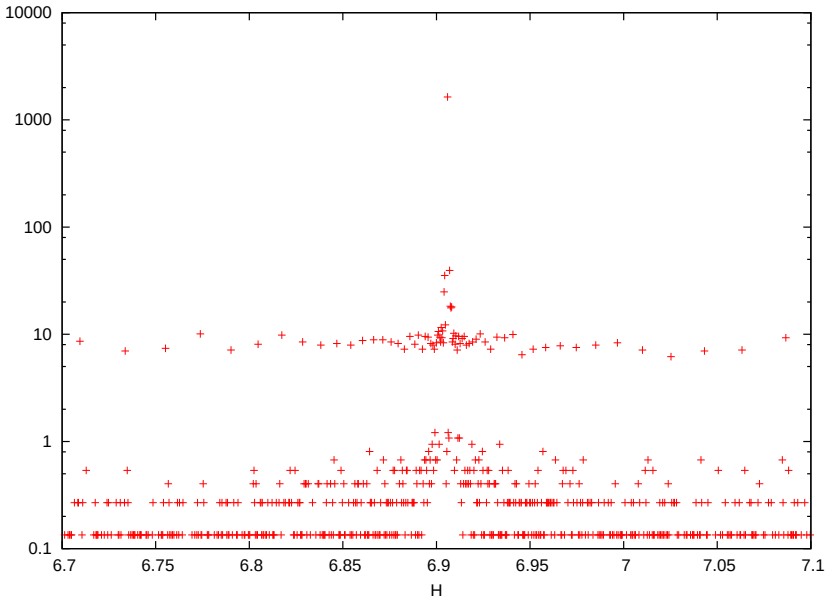

Figure 2.9: Calculated NMR-spectrum with assumed correlation length of $\xi = 7.38$ and $S_0 = 0.15$, 20000 runs and a vacancy density of 0.25%. It has been plotted with logarithmic scale to point out the distinct resonance peaks at equidistant magnetic fields, which show the discrete distribution of magnetization values in the sample.

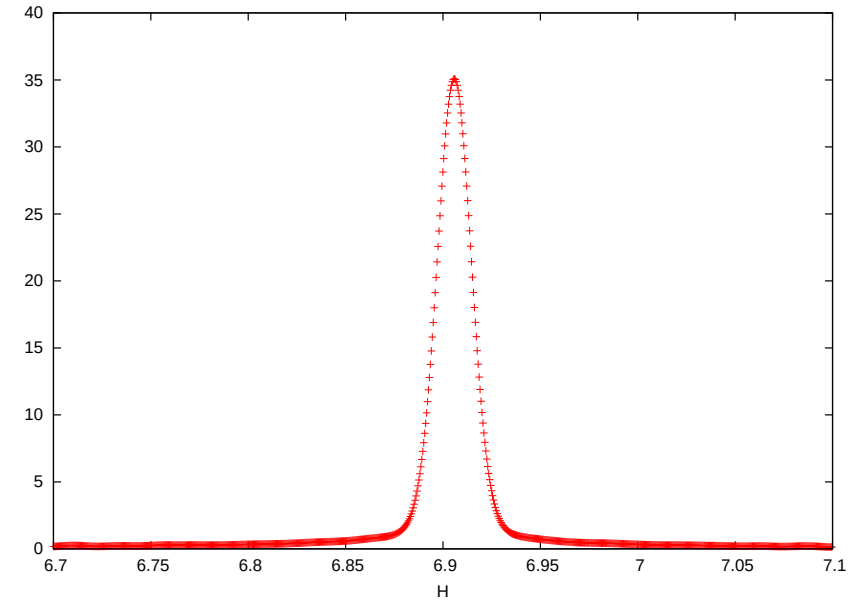

Figure 2.10: Calculated NMR-spectrum with assumed correlation length of $\xi = 7.38$ and $S_0 = 0.15$, 20000 runs and a vacancy density of 0.25%. An additional smearing of $200G$ was applied in order to mimic the natural line-width.

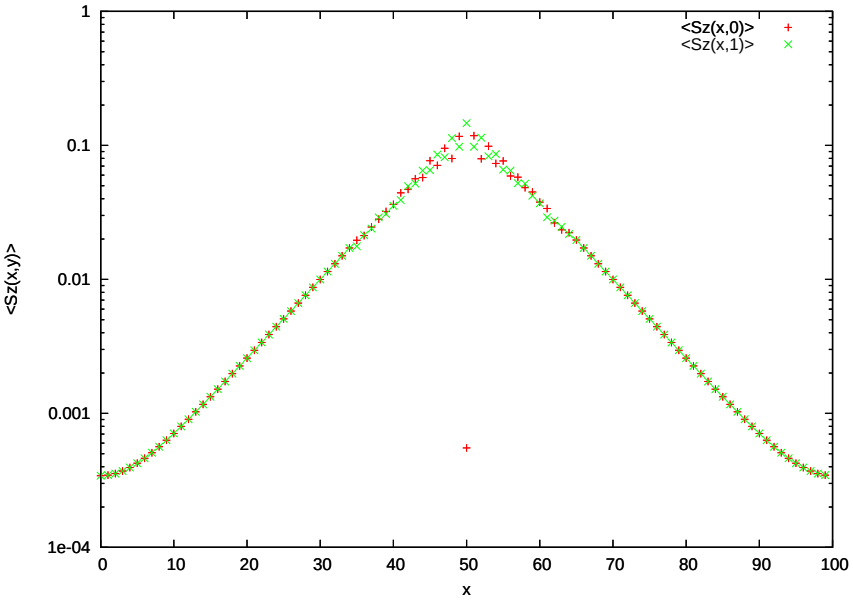

Figure 2.11: Magnetic profile with theoretical assumed behavior outside of a domain $35 < x < 65$ around the vacancy.

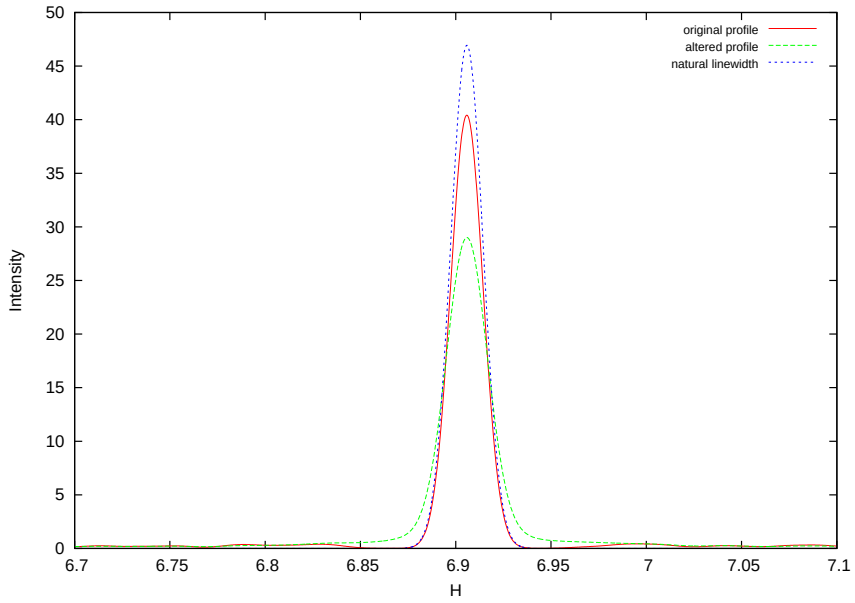

Figure 2.12: NMR spectrum, obtained by using the magnetization profile directly and by using a magnetization profile as pictured in fig. 2.11. Additionally the natural line-width is plotted.

the NMR profile the energy densities of some arrangements of nearby vacant spins were calculated. They were used to determine a weight which was then used to either accept or decline a given vacancy configuration within the NMR-run. Although the energies show significant changes for two neighboring vacancies (see fig. 2.13), no impact on the resulting NMR spectrum was detected for small vacancy densities.

2.2.5 Systematic Approach to Nearby Vacancies

To examine effects of nearby vacancies three major test series were performed for different temperatures. The temperatures $T = 0.025, 0.0625, 0.175$ were chosen to reflect the given measurements of Fujiwara et al., $40K$, $100K$, and $280K$, respectively [3]. Monte Carlo simulations were done for single vacancies and for two vacancies on a 100×2 ladder system with varying distances. They lay up to 40 sites apart on alternating chains.
A total of 108 magnetization profiles were produced, a few samples are shown in figures 2.14, 2.15, 2.16, and 2.17. The difference of the first two pictures is that in the first the two sites lie on the same sub-lattice but they do not in the second. The vacancies are in both cases 8 rungs apart, but on alternating chains. One can clearly see that lying on different sub-lattices destroys the magnetic profile. The effect can be seen by looking at

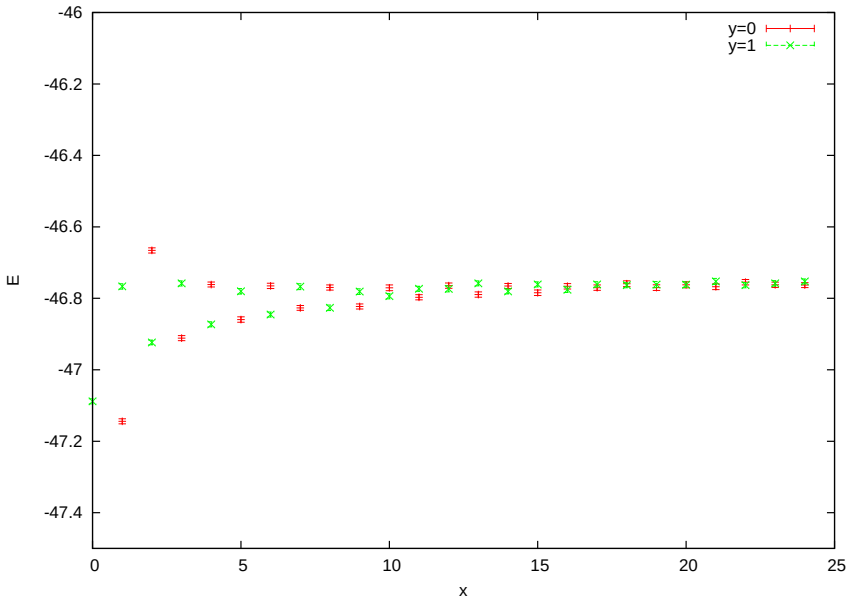

Figure 2.13: System energy depending on the distance of 2 inserted vacancies. The system size was 100×2 and the couplings were $J_\perp/J_\parallel = 0.5$.

the whole set of profiles for vacancy distances up to the order of 1.5 correlation lengths. This has of course large influence on the NMR spectra, meaning that the central peak originating from the *zeros* in the magnetic profile is dominating and the broadening is diminished. Comparing figures 2.16 and 2.17 shows the dependence on the temperature. Higher temperatures also destroy the magnetic profile which is in accordance with the expectations.
So the reduction of the line-width for larger temperatures can be explained (see sec. 1.6.1).

2.2.6 NMR-Spectra

An additional feature of the NMR program was implemented for nearby vacancies. If any two of the random chosen sites for vacancies fell within a certain distance, the spectrum in this area would not be composed by the two single-vacancy spectra but by the respective spectrum for the two vacancies. This allows for possible effects like a strengthening of correlations e.g. between close-by neighboring vacancies. For this test 20.000 vacancy configurations were sampled.
Very little broadening of the NMR spectral line-width could be detected as can be seen in fig. 2.18-2.20 for different temperatures.

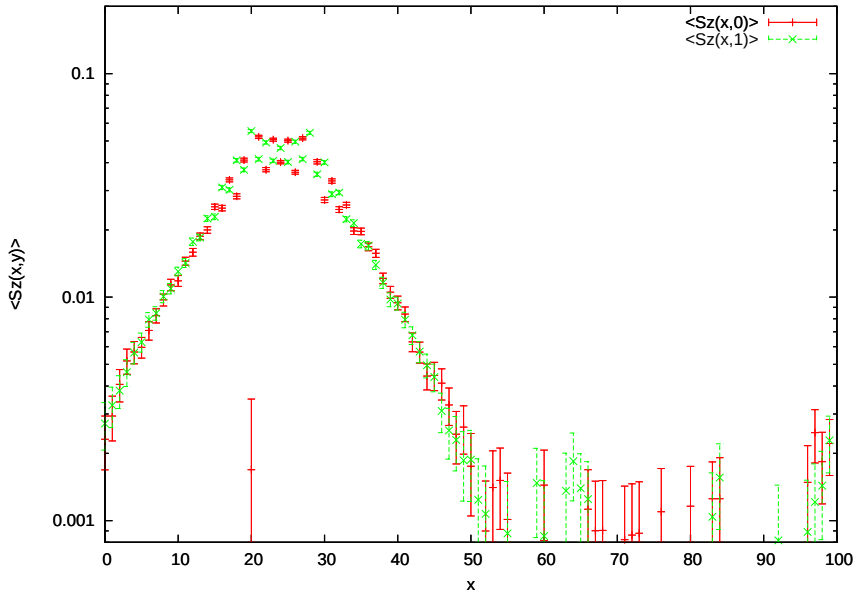

Figure 2.14: Magnetization profile at $T = 0.025$ of a system 100×2 with two nearby vacancies on the same sub-lattice at $(19, 0)$ and $(27, 0)$. The couplings were set to $J_\perp/J_\parallel = 0.5$ and the magnetic field was $h = 0.01$.

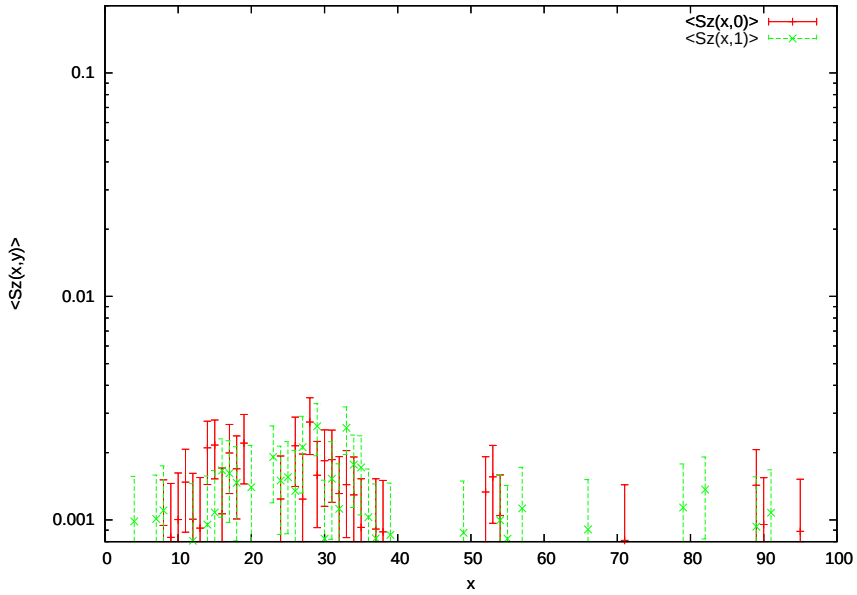

Figure 2.15: Magnetization profile at $T = 0.025$ of a system 100×2 with two nearby vacancies on different sub-lattices at $(19, 0)$ and $(27, 1)$. The couplings were set to $J_\perp/J_\parallel = 0.5$ and the magnetic field was $h = 0.01$.

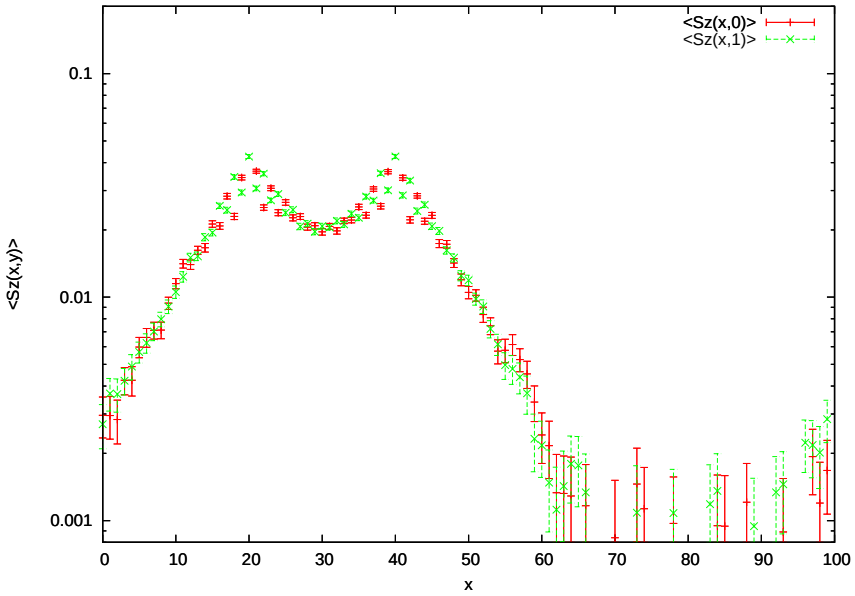

Figure 2.16: Magnetization profile at $T = 0.025$ of a system 100×2 with two vacancies on the same sub-lattice at $(19, 0)$ and $(39, 0)$. The couplings were set to $J_\perp/J_\parallel = 0.5$ and the magnetic field was $h = 0.01$.

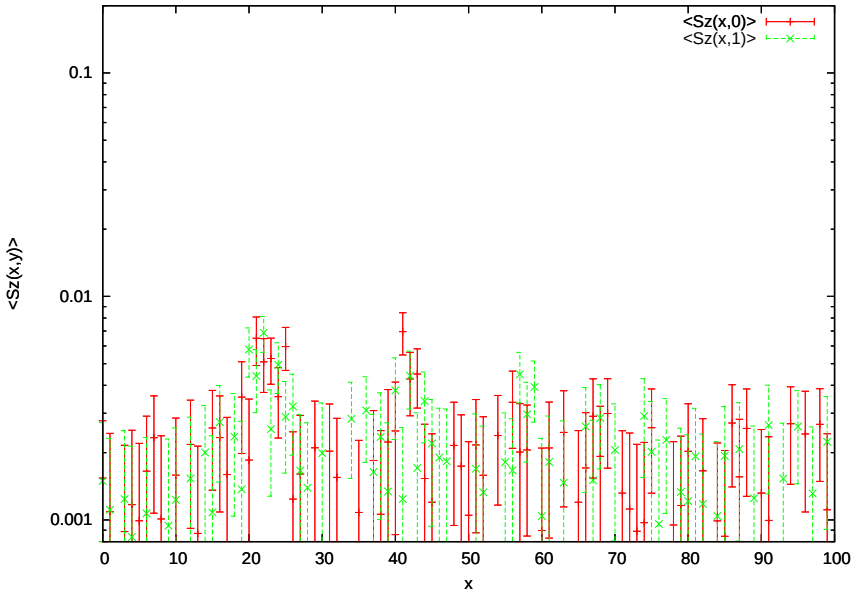

Figure 2.17: Magnetization profile at $T = 0.175$ of a system 100×2 with two nearby vacancies on the same sub-lattice at $(19, 0)$ and $(39, 0)$. The couplings were set to $J_\perp/J_\parallel = 0.5$ and the magnetic field was $h = 0.01$.

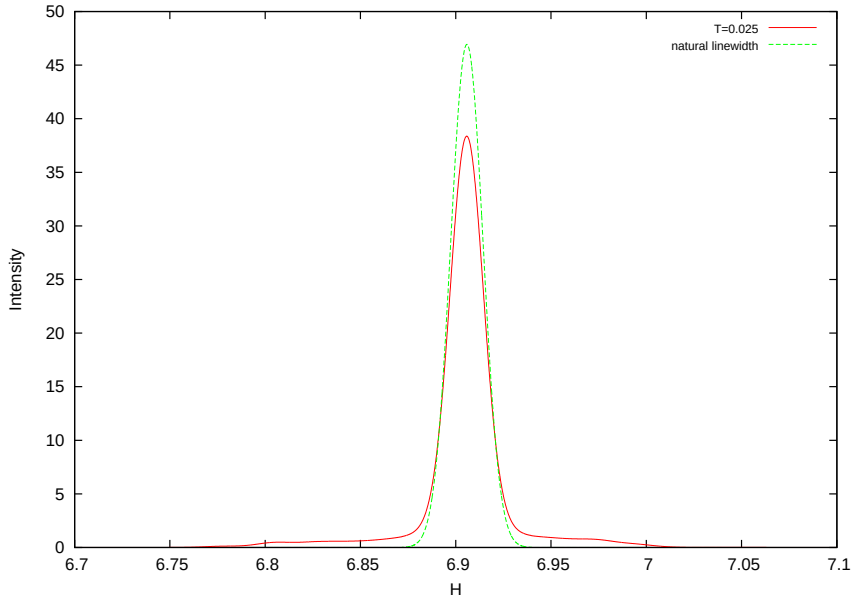

Figure 2.18: NMR spectrum with consideration of nearby vacancies at $T = 0.025$. The vacancy density was set to 0.25 % and 20000 configurations were sampled.

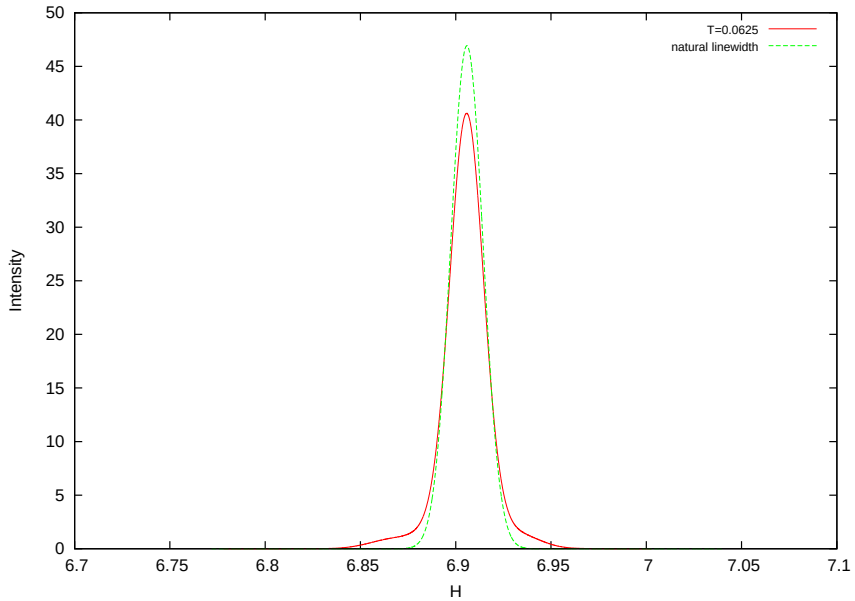

Figure 2.19: NMR spectrum with consideration of nearby vacancies at $T = 0.0625$. The vacancy density was set to 0.25 % and 20000 configurations were sampled.

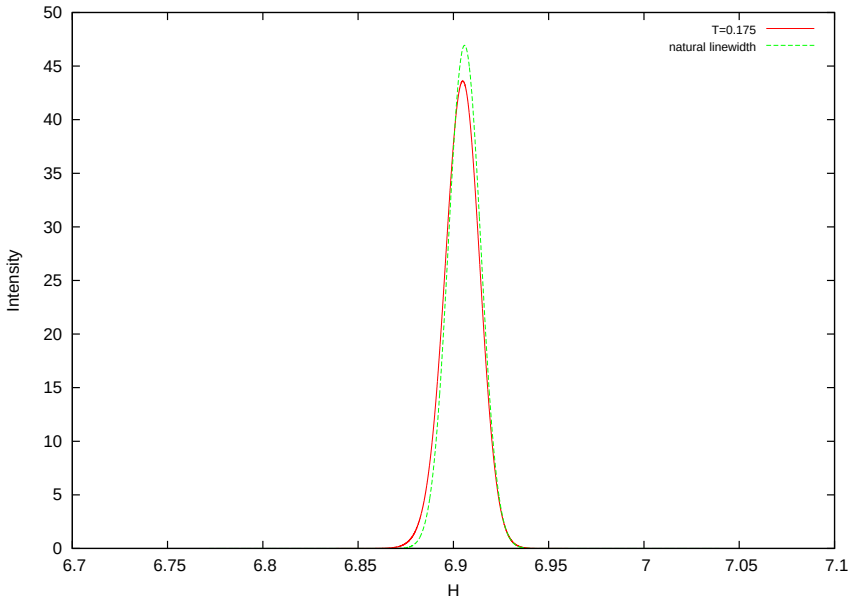

Figure 2.20: NMR spectrum with consideration of nearby vacancies at $T = 0.175$. The vacancy density was set to 0.25 % and 20000 configurations were sampled.

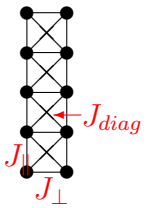

Figure 2.21: Additional spatial diagonal term.

2.3 Diagonal Couplings

An additional ferromagnetic spatial diagonal term (fig. 2.21) on the plaquettes of the ladder was proposed by Johnston et al. (see sec. 1.4.1) to give a more accurate description of the system without considering inter-ladder couplings. Typical values for the interaction strengths are $J_\perp/J_\parallel = 0.5$ and $J_{diag}/J_\parallel = -0.1$.

To determine the influence of such a term on the magnetic profiles and consequently on the NMR profiles, DMRG was used. First, extensive comparisons between small system results obtained from DMRG and from exact diagonalization were performed to ensure accurate implementation. After simulating a series of systems no effects on the magnetic profiles could be detected for diagonal coupling strengths up to $J_{diag} = -0.5$.

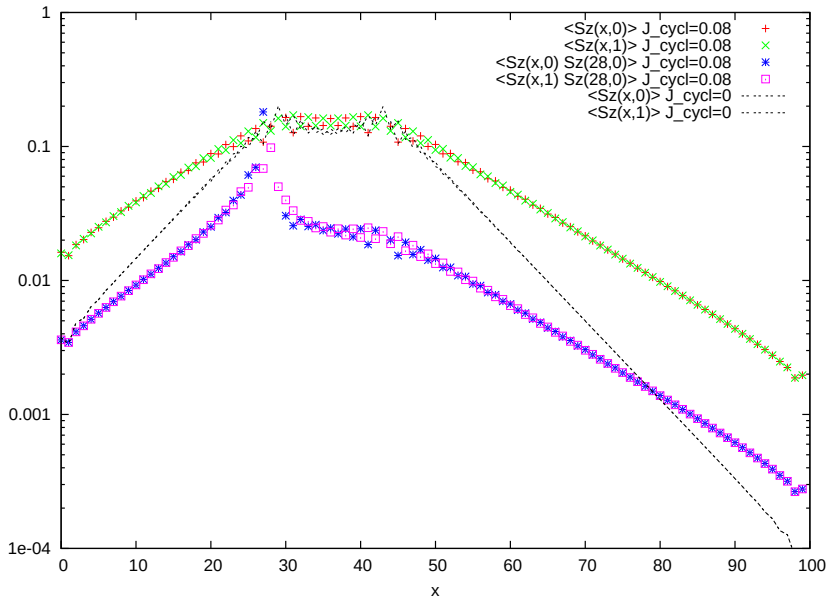

Figure 2.22: Magnetization profile obtained by DMRG of a system with 2 vacancies 19 rungs apart on a ladder with cyclic exchange couplings $J_\perp/J_\parallel = 0.77$, $J_{diag}/J_\parallel = 0.015$, and $J_{cycl}/J_\parallel = 0.08$. Additional the magnetization for the system without cyclic exchange term and $J_\perp/J_\parallel = 0.5$ is plotted for comparison.

2.4 Cyclic Exchange Term

Another possible origin of enhanced correlations needed to explain experimental data is a possible cyclic exchange term (see sec. 1.2.2). Comparing the results of small system experiments with exact treatment of the Hamiltonian ensured correct implementation. Further tests were done with a parameter set proposed by Johnston [1]: $J_\parallel/k_B = 2260(60)K$, $J_\perp/J_\parallel = 0.77(12)$, $J_{diag}/J_\parallel = 0.015(10)$, and $J_{cycl}/J_\parallel = 0.092(13)$. As can be seen in profile 2.22 an enlargement of the correlation length is being achieved. It increased up to values of $\xi = 15(1)$ which almost doubles the correlation length from prior systems.

The drawback is that the spin-gap of the system does not fit to the experimental data, in contradiction to the suggested behavior by Johnston.

Although the enlargement is necessary to get broader NMR spectra this does not explain the discrepancy of experimental effects on the unperturbed ladders and on doped ladders (see sec.1.6.1).

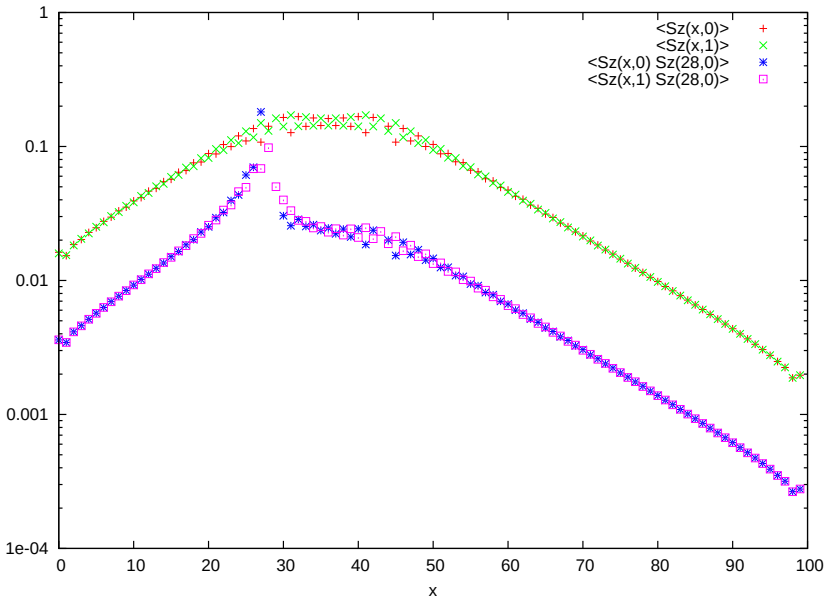

Figure 2.23: Magnetization profile and correlations obtained by DMRG of a system with 2 vacancies 14 rungs apart on a ladder with cyclic exchange couplings.

Another possible way out of this contradiction was detected in fig. 2.23. As can be seen the magnetization is stabilized between the vacancies on an almost constant level. If this effect leads to a larger amount of sites with large magnetization values this would broaden the NMR spectrum. So again a series of simulations for different distances was performed and the NMR program was fed with this data, but no additional broadening could be detected (see fig. 2.24). The phenomenon could be reduced to a very local effect and the presence of a larger correlation length.

2.5 Excitation Spectra

In order to get a good overview of the dynamics of a given system, some excitation spectra were produced representing many typical cases. This was achieved by measuring the imaginary time correlations and then decomposing the Green's function into the dynamic structure factor (see eq. 1.19).

$$G(\tau) = \int_0^\infty S(\omega)\exp\left(-\omega\tau\right) d\omega \tag{2.1}$$

The dynamic structure factor was plotted in (k, ω)-space where k represents the momentum and ω the real-space frequency.

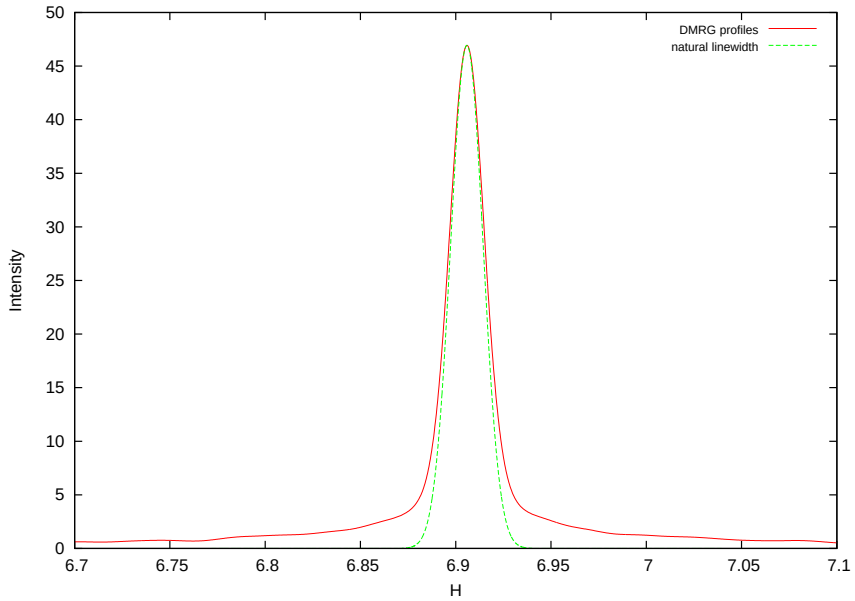

Figure 2.24: NMR spectrum obtained by using DMRG magnetization profiles of nearby vacancies including a cyclic exchange term.

The plot for the basic ladder system is shown in fig. 2.25. The spectrum shows typical ladder-like properties, mainly the finite spin-gap at $k = \pi$. Furthermore it exhibits a sinusoidal behavior which corresponds to the dispersion relations of the elementary excitations, the spinons. The continuity of the spectrum can be explained by the creation of *two* spinons for each excitation. The energy is then distributed among those [11].

A single vacancy on the ladder changes the spectrum in a way as can be seen in fig. 2.26. A new mode is introduced at zero frequency and momentum π. See fig. 2.27 for the relative intensity of the new mode plotted vs. momentum. Roughly speaking, this reflects the behavior of the induced spin by the vacancy, which can be flipped without energy cost.

Further tests included the insertion of more than one vacancy. As can be seen in figure 2.28 the spectrum is relatively unchanged by adding a vacancy next to the first one. For two vacancies of distance up to 20 the excitation mode at $\omega = 0$ is clearly visible, too (see fig. 2.29).

Also some spectra with small magnetic field were produced, but no more results with substantial differences were achieved.

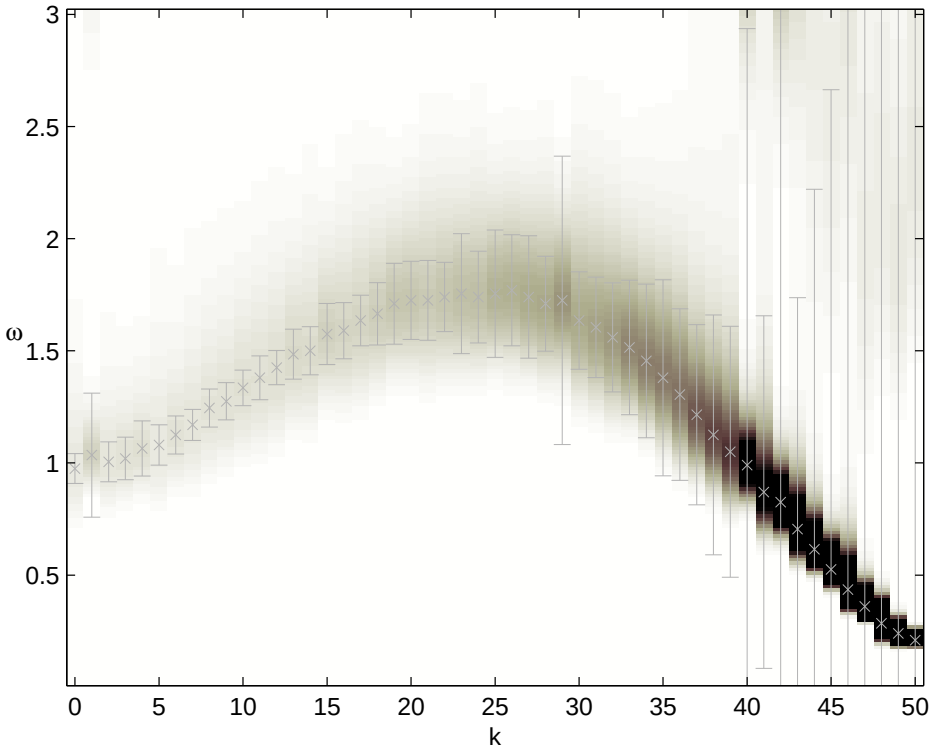

Figure 2.25: Excitation spectrum of a 100×2 ladder system. $k = 50$ corresponds to momentum π.

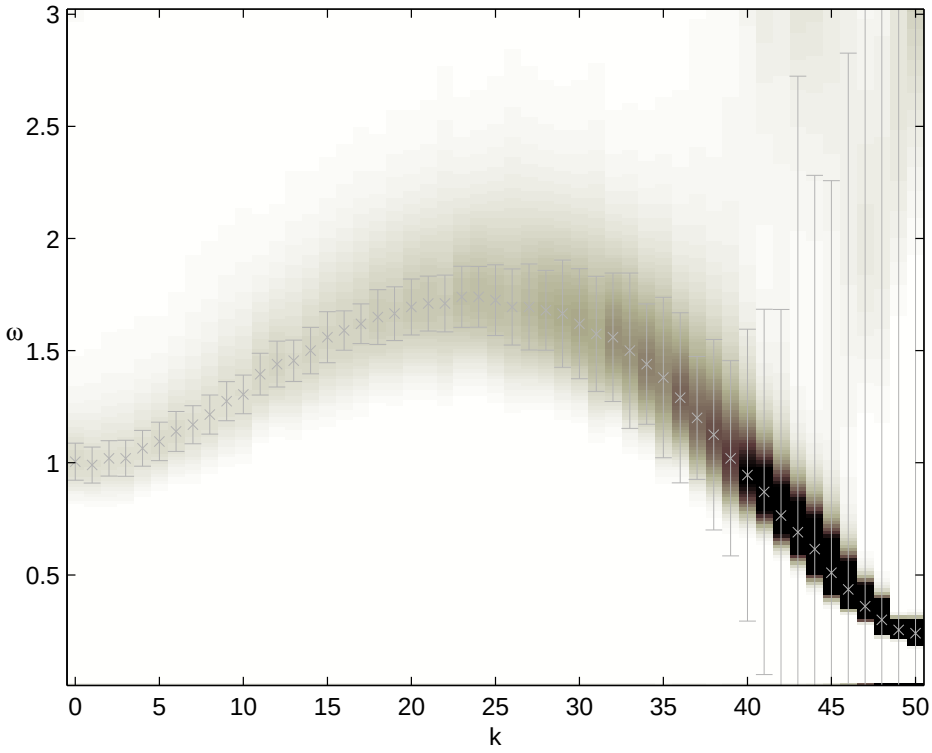

Figure 2.26: Excitation spectrum of a 100×2 ladder system including 1 vacancy. $k = 50$ corresponds to momentum π. Note the additional mode at $\omega = 0$ originating from the insertion of the vacancy.

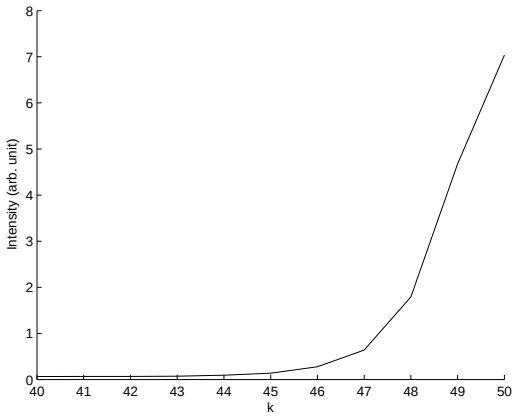

Figure 2.27: Relative intensity of the excitation mode originating from the insertion of the vacancy (see fig. 2.26).

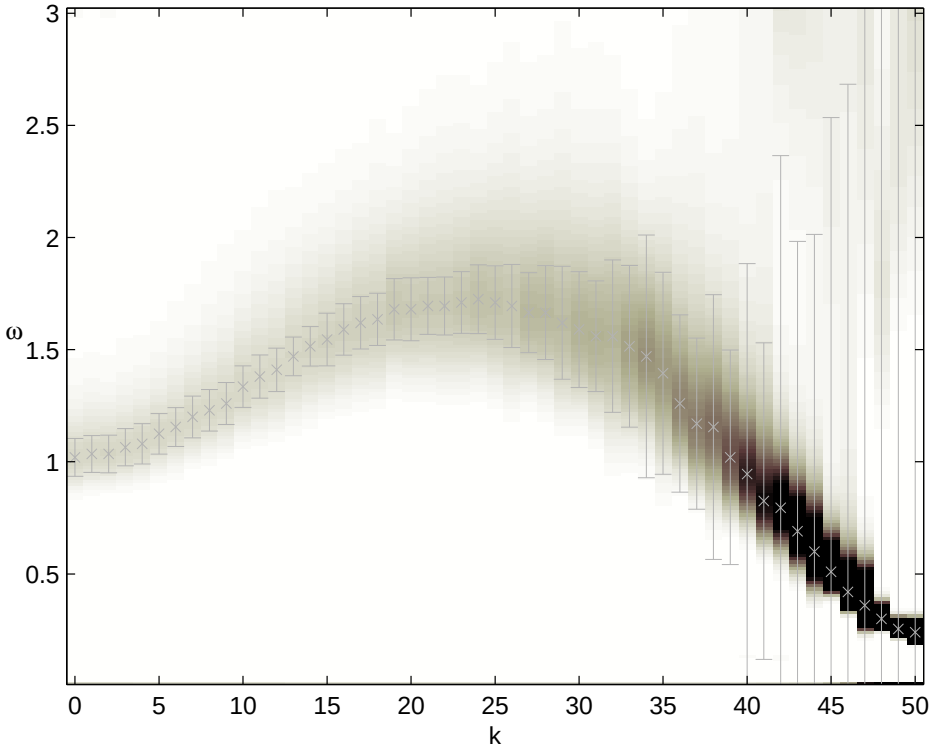

Figure 2.28: Excitation spectrum of a 100×2 ladder system with 2 vacancies next to another on different sub-lattices. $k = 50$ corresponds to momentum π. Note the additional mode at $\omega = 0$ originating from the insertion of the vacancies.

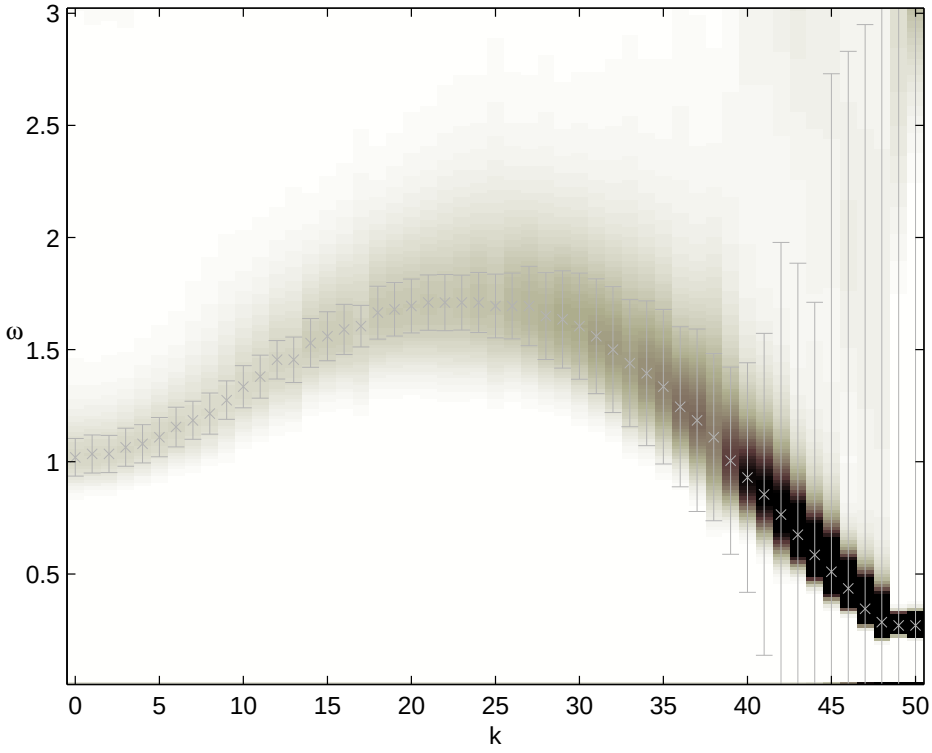

Figure 2.29: Excitation spectrum of a 100×2 ladder system with 2 vacancies on the same sub-lattice of distance 20 apart from each other. $k = 50$ corresponds to momentum π. Note the additional mode at $\omega = 0$ originating from the insertion of the vacancies.

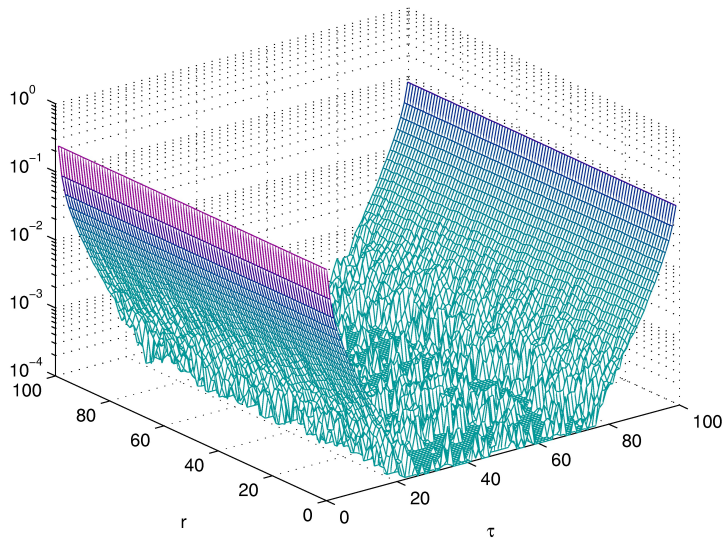

Figure 2.30: Correlations for each site r in imaginary time τ for a 100×2 ladder system.

2.6 Correlation Analysis

To learn more about the correlations in the material in momentum and frequency space as well as in real space some plots were produced. The emphasis lied on comparing systems with and without vacancies, concluding that their existence has quite an impact on the outcoming picture.

Figure 2.30 shows the correlations in imaginary time for each site for a simple ladder system, whereas fig. 2.31 is the same plot with an additional vacancy at site 50. The correlations in imaginary time have a non-vanishing part. This is a further indication for the free spin because this feature is exactly expected from an unpaired spin. Also one sees the distribution of the *spin-cloud* around the vacancy in a definite, exponentially limited area.

The whole extension of the impact of the vacancy insertion on the entire system can be seen in the following plots. Figure 2.32 shows a simple retransformation of the correlations in momentum space back into real space, which means that the spatial axis denotes the distance of each site to another. This figure shows the output not only for the simple system without vacancy but also the system with one vacancy and so a comparison can be made. The correlations break clearly the symmetry of space-time. This is not surprising since the insertion of a vacancy also breaks this symmetry: it is

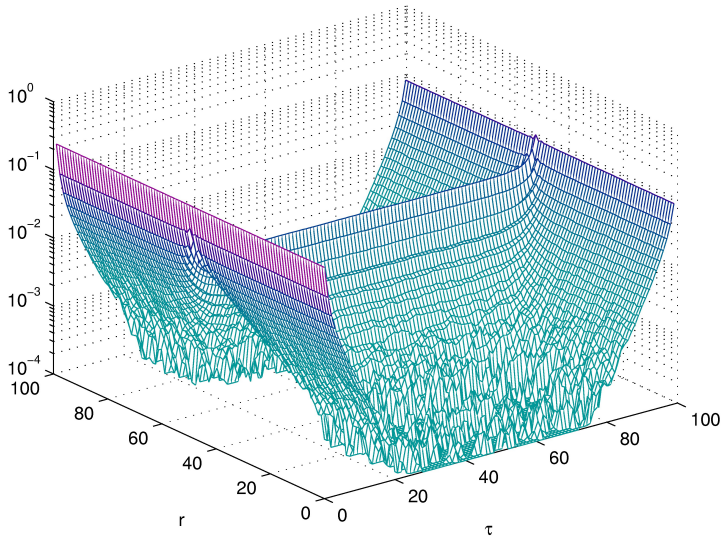

Figure 2.31: Correlations for each site r in imaginary time τ for a 100×2 ladder system with a single vacancy at $x = 50$.

on one single site for all times.

The same comparison for the system with two neighboring vacancies on one chain of the ladder shows rather surprising results. As can be seen in fig. 2.33 the addition of a second vacant site annihilates the presence of the first one. The plot looks perfectly like the plot of the simple ladder. One could probably say that the two induced spins annihilate themselves.

2.7 Susceptibility

The temperature-behavior of the susceptibility indicates the nature of an interaction [37]. Recalling the resonating valence-bond picture of sec. 1.3 and the picture of a spin distributed around a vacancy one is able to determine an effective interaction between such induced spins by observing the susceptibility.

Uniform and staggered susceptibilities were calculated for a 100×2-sized system with no, one and two vacancies on the same and different sub-lattices, respectively.

To eliminate the influence of the lattice itself the value for the pure lattice was subtracted.

The susceptibilities were calculated for temperatures from $T = 0.001$ up to $T = 50$.

Fig. 2.34 shows the clearly different behavior of the system with vacancies on different

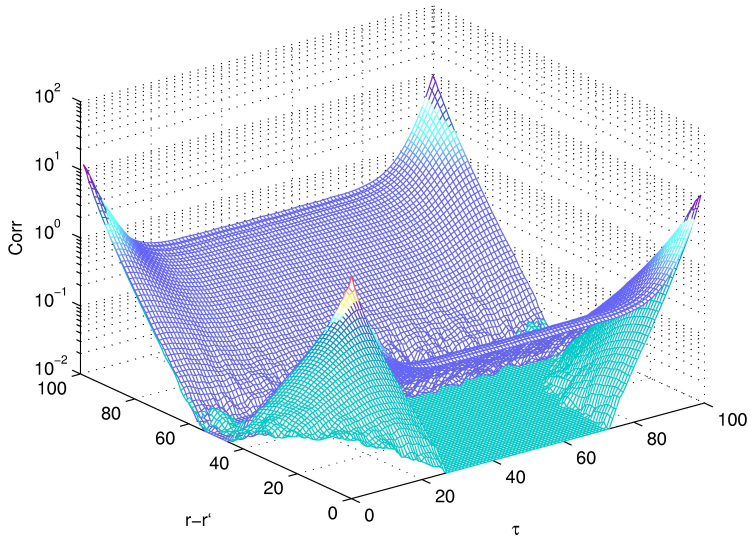

Figure 2.32: Correlations as a function of distance $r - r'$ in real space and in imaginary time τ. A simple 100×2 ladder system and the same system with a single vacancy are compared.

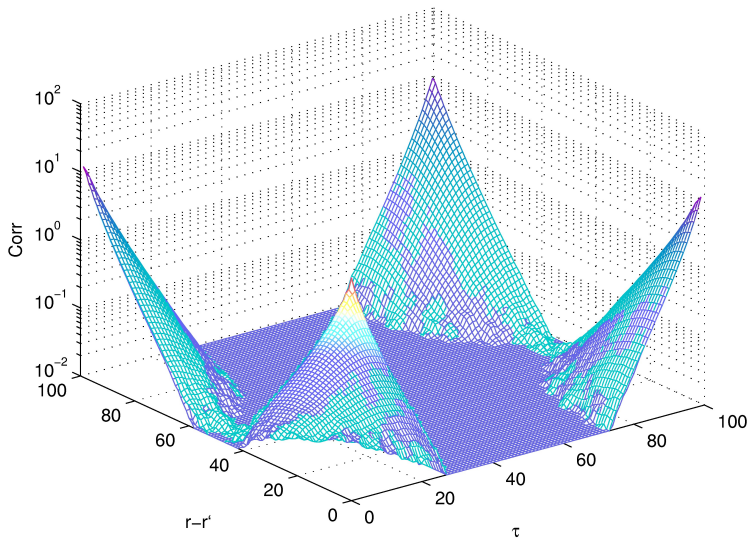

Figure 2.33: Correlations as a function of distance $r - r'$ in real space and in imaginary time τ. A simple 100×2 ladder system and the same system with two nearby vacancies on different sub-lattices are compared.

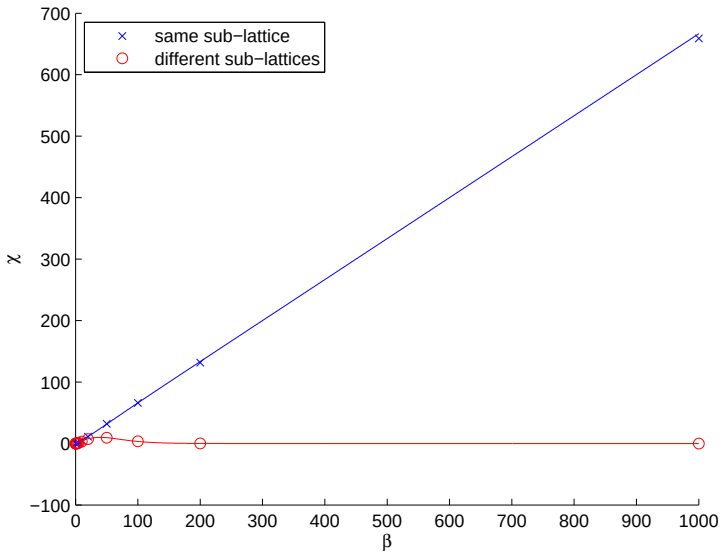

Figure 2.34: Part of the uniform susceptibility originating from the vacancies for a system with two vacancies 14 rungs apart lying on the same sub-lattice and on different sub-lattices plotted versus the inverse temperature β.

sub-lattices compared with vacancies on the same sub-lattice. The values were fitted with the theoretical behavior of the uniform susceptibility of two spins coupled with an effective coupling J_{eff}:

$$\chi = \frac{2\beta}{3 + e^{\beta J_{\text{eff}}}} \tag{2.2}$$

The effective coupling between vacancies on the same sub-lattice turned out to be of ferromagnetic nature ($J_{\text{eff}} = -0.028(5)$) while for the system with vacancies on different sub-lattices it turned out to be anti-ferromagnetic ($J_{\text{eff}} = 0.045(5)$).
This confirms previous results of magnetization profiles of systems with two vacancies which add-up to another for lying on same and destroy each other for lying on different sub-lattices.

2.8 Spin Anisotropy

Another possibility of altering the model to get a more accurate description of the material is the introduction of a spin-anisotropy. In contrast to the Heisenberg model of sec. 1.2.1 the coupling strength connecting the z-component and the $x-$ and $y-$

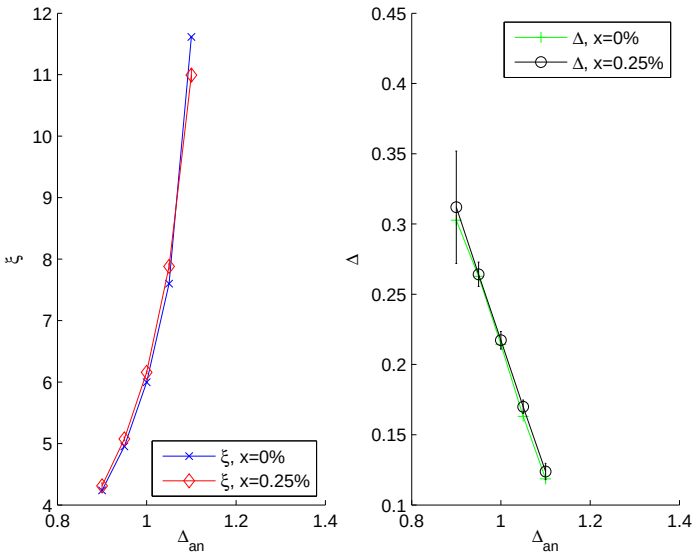

Figure 2.35: Influence of introducing a spin anisotropy to the Heisenberg model on the correlation length (ξ) and spin-gap (Δ) of a ladder system for vacancy densities $x = 0\%$ and $x = 0.25\%$.

components of the spin operators are different:

$$H = J \sum_{\langle i,j \rangle} \left(\frac{1}{2} \left(S_i^+ S_j^- + S_i^- S_j^+ \right) + \Delta_{an} S_i^z S_j^z \right) + h \sum_i S_i^z \tag{2.3}$$

with $\Delta_{an} \neq 1$.

Some calculations were done for a ladder system (100×2) without vacancies and the usual $J_\perp / J_\parallel = 0.5$ coupling ratio for the inter-ladder interactions. Measuring the same-time correlations as well as the imaginary time correlations at momentum $k = \pi$ at temperature $T = 0.025$ and fitting them with the appropriate model function led to figure 2.35. Also shown are the according plots with a vacancy density of $x = 0.25\%$. The values for the spin-gap and the correlation length of this system are means over 40 independent vacancy configurations.

As can be seen in this table the spin-gap decreases in the same way the correlation length increases. Additionally the influence of low vacancy concentration is quite small, actually it falls within error margins. Therefore this particular model cannot be used to describe a system with the same gap but larger spatial correlations and a substantial change when inducing vacancies.

2.9 Conclusions

A series of simulations have been done on a single ladder using the Heisenberg model including diagonal and cyclic exchange terms. The excitation spectra and the correlation plots show the impact of vacancies on the ladder system. But the broadening of the NMR spectrum shown in experiments by Fujiwara et al. (see sec. 1.6.1) cannot be described with the above indicated model.

3 Results: Stacked Ladders

The major topic of this chapter is to examine the influence of the inter-ladder coupling perpendicular to the ladder planes. A way of looking at the system is that of two anisotropic coupled planes. Work has been done on this system before although focus was not laid on the coupling strengths necessary for the system described here.
Sandvik and Scalapino [38] studied the anti-ferromagnetic order-disorder transition in a two-layer Heisenberg anti-ferromagnet by stimulating the inter-plane coupling strength. While the single 2D Heisenberg plane is in an ordered phase at $T = 0$ the coupled planes undergo a phase-transition at a critical inter-plane coupling of $J_c/J_{\text{in-plane}} = 2.51(2)$. The transition is consistent with the classical 3D Heisenberg universality class. The disordered phase above the critical point has an excitation gap and a finite correlation length.
Sengupta et al. [39] examined two coupled planes with anisotropic interactions inside the layers. They found a square-root dependence of the critical inter-layer coupling on the anisotropy of the couplings in the planes.
The presence of a phase transition with critical couplings close to the actual couplings in the sample could lead to effects which stimulate the magnetization of the system. At first, this chapter deals with efforts to find and classify the transition. Then the influence of vacancies on the magnetization and on NMR spectra is examined.

3.1 The Quantum Critical Point

3.1.1 QMC Calculations

For an extensive analysis of the the quantum critical point (QCP) of the stacked ladder system the ideas of Sengupta et al. [39] were followed.
System sizes of $32 \times 2 \times 8$, $40 \times 2 \times 10$, $48 \times 2 \times 12$, and $56 \times 2 \times 14$ were used. The relative extensions in x- and z-direction which correspond to the ladder and stacking direction were chosen to reflect the spin-wave velocities in both directions, which gives

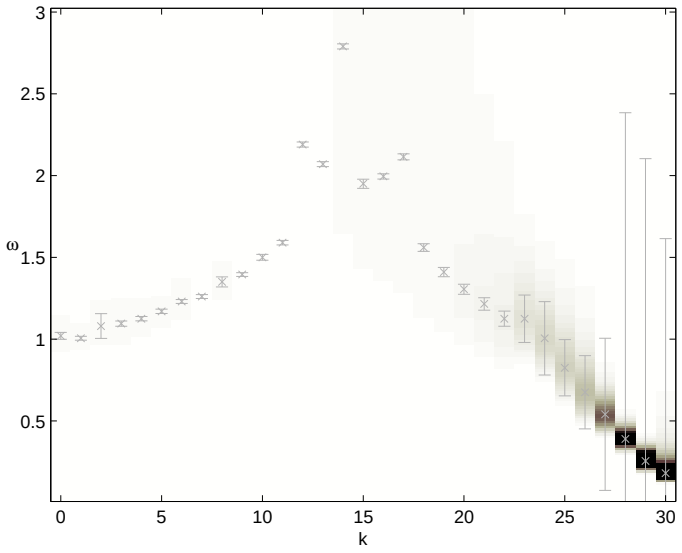

Figure 3.1: Excitation spectrum of a $60 \times 2 \times 6$ stacked ladder system with inter-ladder coupling strength $J_3/J_\parallel = 0.02$. $k = 30$ corresponds to momentum π.

the possibility of avoiding effects described by Sandvik [40], which may lead to false conclusions performing a FSS analysis (see sec. 1.7.9).

3.1.2 Excitation Spectra

For the stacked ladder system the excitation spectra reflect the appearance of a phase transition to an ordered phase at a critical coupling in stacking direction of about $J_3/J_\parallel = 0.05$ when choosing $J_\perp/J_\parallel = 0.5$ accordingly to sec. 1.4.1. In figures 3.1, 3.2, and 3.3 this behavior is clearly visible as a part of the spectral weight at $k = \pi$ emerges from the main peak and moves towards $\omega = 0$ for increasing coupling. The remaining part, which stays almost constant for all couplings at the value of the spin-gap of the pure ladder indicates a further time scale originating from the dynamics of the ladder itself (see fig. 3.4).

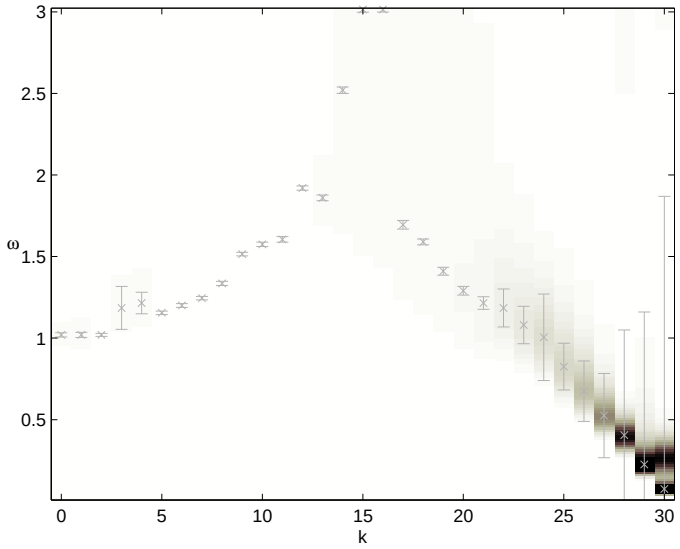

Figure 3.2: Excitation spectrum of a $60 \times 2 \times 6$ stacked ladder system with inter-ladder coupling strength $J_3/J_{\parallel} = 0.04$. $k = 30$ corresponds to momentum π.

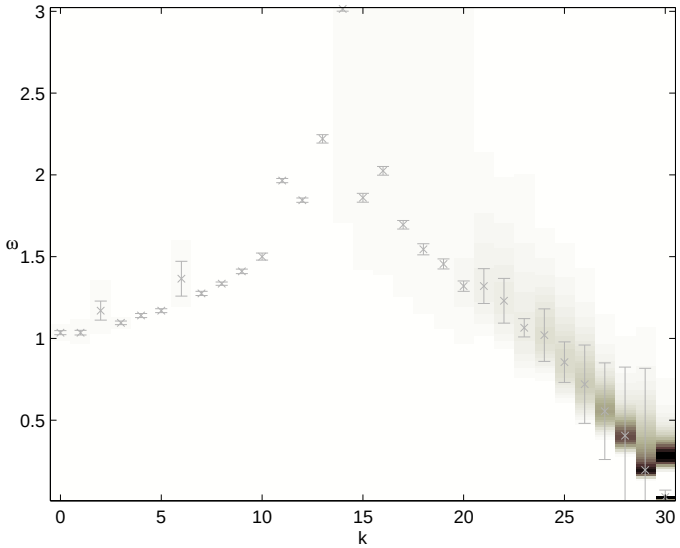

Figure 3.3: Excitation spectrum of a $60 \times 2 \times 6$ stacked ladder system with inter-ladder coupling strength $J_3/J_{\parallel} = 0.06$. $k = 30$ corresponds to momentum π.

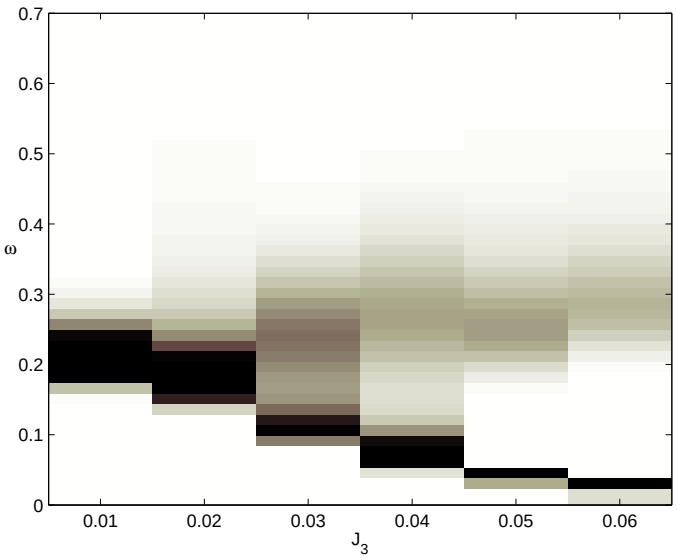

Figure 3.4: Excitation spectrum of a $60 \times 2 \times 6$ stacked ladder system at momentum (π, π, π) for different couplings $J_3/J_\parallel$.

3.1.3 The Critical Coupling

A convenient method of determining the exact coupling strength at the critical point is the usage of the *spin stiffness*. It is defined as

$$\rho = \frac{\partial^2 F(\phi)}{\partial \phi^2} \tag{3.1}$$

where $F(\phi)$ is the free energy per site and ϕ determines a *twist* acting on the spins. There is an improved estimator for this value, which relates the stiffness to the world-line winding number [41]. For each dimension the relation reads

$$\rho_x(T) = \frac{L_x^2}{N\beta} \langle W_x^2 \rangle \tag{3.2}$$

where W_x is the winding number in x-direction, L_x denotes the number of sites in this direction, and N the number of all sites. A finite size scaling analysis (see sec. 1.7.9) reveals a scaling law for this observable

$$\rho(L) \propto L^{d-2-z} \tag{3.3}$$

where d is the dimension and z the dynamical critical exponent which is set to 1 according to the classical 3D Heisenberg universality class. So plots of $L\rho$ versus the coupling strength for different system sizes should intersect exactly at the quantum critical point.

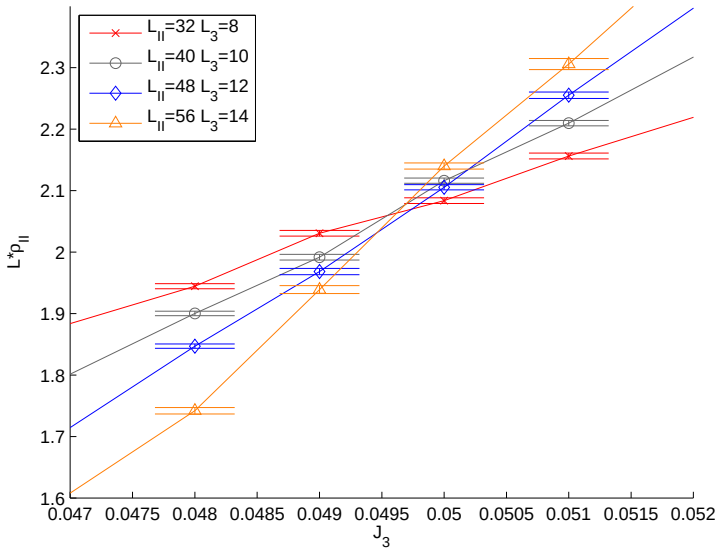

Figure 3.5: Scaling plot for the spin stiffness in ladder direction to determine the critical coupling.

Following the argumentation of Sengupta et al. [39] an analysis of this kind for both spatial directions gives rise to the possibility of an error estimation because of opposite directions of convergence.
This method was used to get the critical coupling of a stacked ladder system without vacancies. The results given in fig 3.5 and 3.6 lead to a critical coupling of $J_3^{crit} = 0.0495(5)$.

3.1.4 The Order Parameter

A suitable order parameter for the ordered phase above the critical coupling was found in the staggered structure factor, which is defined as follows [38]:

$$S_\pi = \frac{1}{N} \sum_{i,j} \langle S_i^z S_{i+j}^z \rangle \, (-1)^{x_i+y_i+z_i+x_j+y_j+z_j} \tag{3.4}$$

where the parity factor includes the coordinates (x_i, y_i, z_i) of a given site and N is the number of all sites. The magnetization is connected to the structure factor by

$$m(L) = \sqrt{\frac{3S_\pi(L)}{2L^2}} \tag{3.5}$$

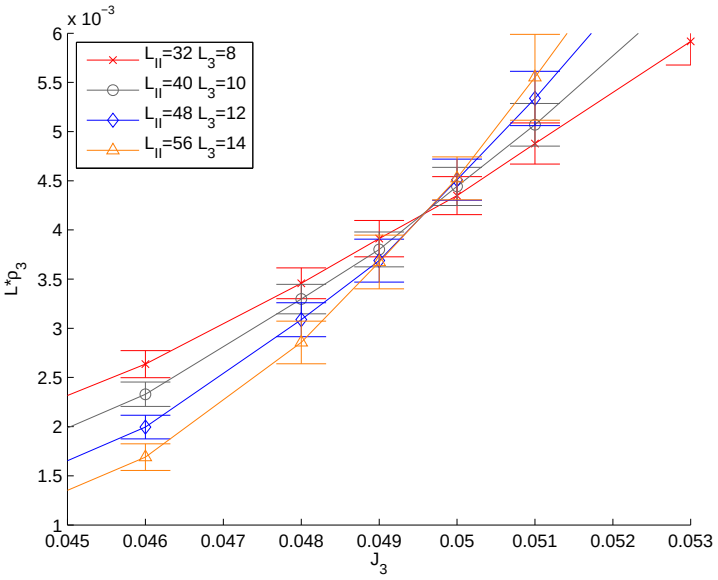

Figure 3.6: Scaling plot for the spin stiffness in stacking direction to determine the critical coupling.

where L is the linear system size. This relation relies on neglecting the short-range fluctuations of spin-spin correlations and is therefore only valid in the thermodynamic limit. But it can be seen as a definition for finite size systems.

A possible way to study the behavior of the magnetization near the critical point is an extrapolation of the finite size magnetizations to the infinite system size. The extrapolation can be seen in fig. 3.7. One can obtain the relation by looking at the theoretical form of the spin-spin correlation function [38]:

$$m^2(L) = m^2(\infty) + c\frac{1}{L^{1-\eta}} \qquad \text{for} \quad m^2(\infty) > 0 \tag{3.6}$$

where $m^2(L)$ is the magnetization for linear size L, c is a constant, and the critical exponent η of the correlation function was set to $\eta = 0.03$ according to the 3D-AF Heisenberg universality class. Plotting the magnetizations versus the couplings leads to fig. 3.8, which shows the known power-law behavior near the critical point:

$$m(j) = j^{\beta} \tag{3.7}$$

where j is a reduced coupling strength of the form $j = (J - J^{crit})/J^{crit}$.

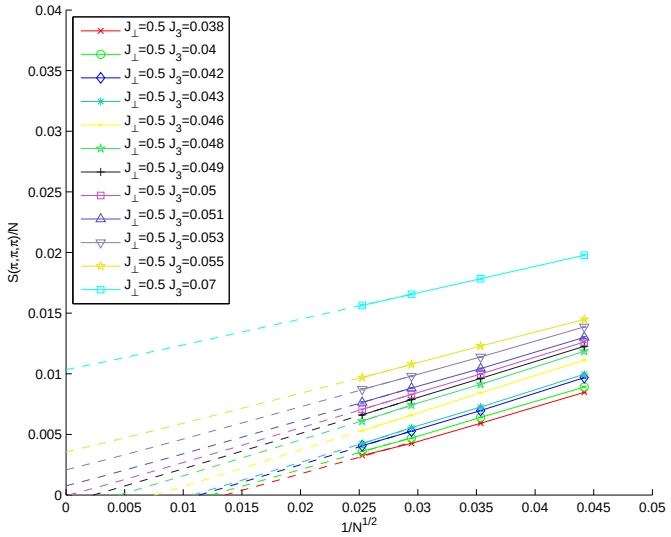

Figure 3.7: Extrapolation of the Magnetization up to infinite size for different coupling strengths $J_3/J_\parallel$ using relation 3.6. For the systems with couplings below the critical point with $m(\infty) < 0$, exponential corrections would have to be applied to get $m(\infty) = 0$.

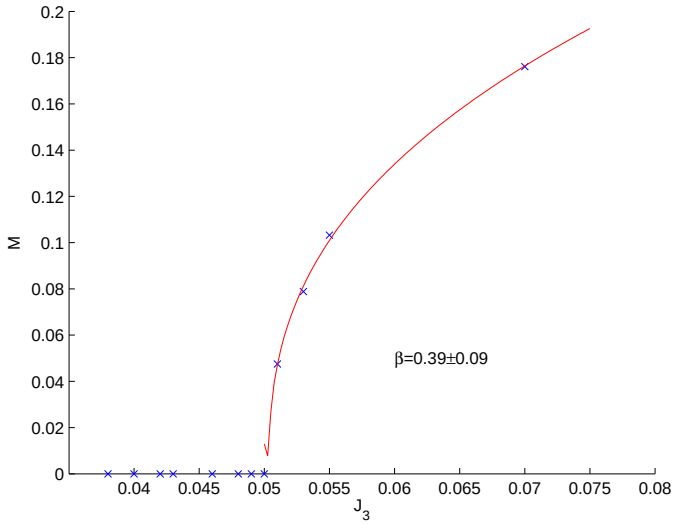

Figure 3.8: Magnetization vs. coupling strength, the critical point is clearly visible. The solid curve represents a power-law fit function with critical exponent β. The critical coupling was set to $J_3^{crit} = 0.0495$ according to sec. 3.1.3. The result $\beta = 0.039(8)$ fits into the classical 3D Heisenberg universality class.

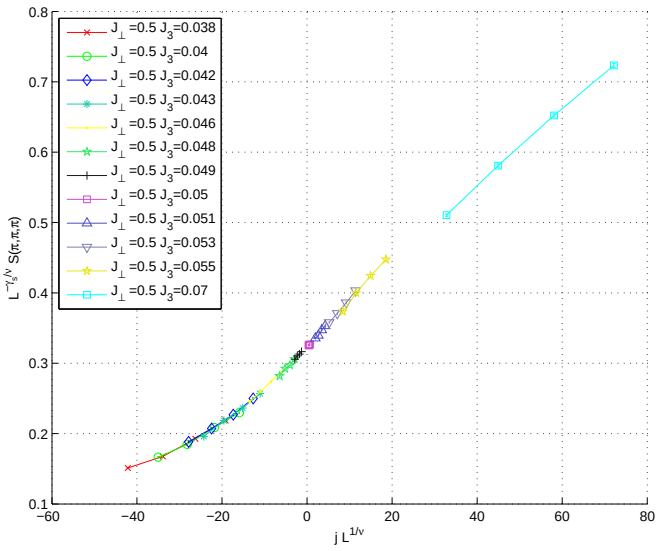

Figure 3.9: FSS-plot for the critical exponents $\gamma_s = 0.66$ and $\nu = 0.71$.

3.1.5 Critical Exponents

For extracting the critical exponents a more sophisticated method exists: the finite size scaling analysis (see sec. 1.7.9). Fig. 3.9 shows such an analysis by plotting $L^{-\gamma_s/\nu} S(\pi, \pi, \pi)$ versus $L^{1/\nu} j$ where j is the reduced coupling strength and γ_s and ν are the critical exponents for the structure factor and the correlation length, respectively. Although there is a constant part in the correlation function above the critical coupling, the dominating effect is that of the staggered structure factor, due to limited system sizes. So a finite size scaling plot delivers an estimator for the critical exponent γ_s only. Furthermore it is insensitive to the exponent ν. The resulting value $\gamma_s = 0.66$ is in good accordance with the one obtained by using the scaling law eq. 3.8 and the exponents of the classical 3D-Heisenberg AF of $\nu = 0.71$ and $\eta = 0.03$.

Some scaling laws show the differences in critical behaviour of physical observables [14]:

$$\gamma_s = \nu(1 - \eta) \qquad \text{Structure Factor} \tag{3.8}$$

$$\gamma_\xi = \nu(2 - \eta) \qquad \text{Susceptibility} \tag{3.9}$$

$$2\beta = \nu(1 + \eta) \qquad \text{Magnetization} \tag{3.10}$$

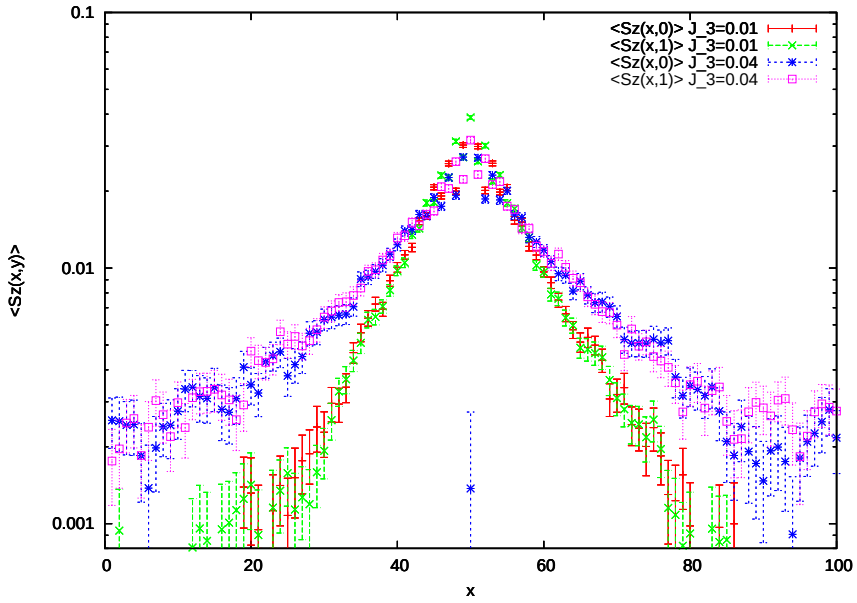

Figure 3.10: Absolute magnetization for coupling strength in stacking direction $J_3/J_\parallel = 0.01$ and $J_3/J_\parallel = 0.04$. The system sizes were $100 \times 2 \times 10$ and $120 \times 2 \times 8$, respectively. The increasing correlation length is clearly visible.

3.2 Vacancies

Johnston et al. [1] predicted a coupling strength of $J_3/J_\parallel = 0.01(2)$ in stacking direction and the usual $J_\perp/J_\parallel = 0.5$ for the intra-ladder couplings for $SrCu_2O_3$. Bearing this in mind a series of Monte Carlo simulations was performed partly on a $100 \times 2 \times 3$, $100 \times 2 \times 10$, $120 \times 2 \times 8$ and on a $200 \times 2 \times 3$ system with third dimension couplings of $J_3/J_\parallel = 0.01$, $J_3/J_\parallel = 0.02$, $J_3/J_\parallel = 0.03$, $J_3/J_\parallel = 0.05$, and $J_3/J_\parallel = 0.1$. The temperature was fixed to $T = 0.025$ which corresponds to about $40K$ in order to focus on the possible broadening at lower temperatures. One vacancy was introduced to analyze possible influence as well on the ladder as on neighboring ones.

Magnetic Profiles for $J_3/J_\parallel = 0.01$ and $J_3/J_\parallel = 0.04$ are depicted in fig. 3.10.

The effect on the NMR profiles is rather small. The profiles don't show the experimentally observed peak broadening (see fig. 3.11).

Additionally some test were done with 2 vacancies on neighboring ladders (see fig. 3.12). It was suggested that additional stabilization of the AF phase between the vacancies would be introduced. No such effect was detected in the corresponding NMR spectrum, either (fig. 3.13).

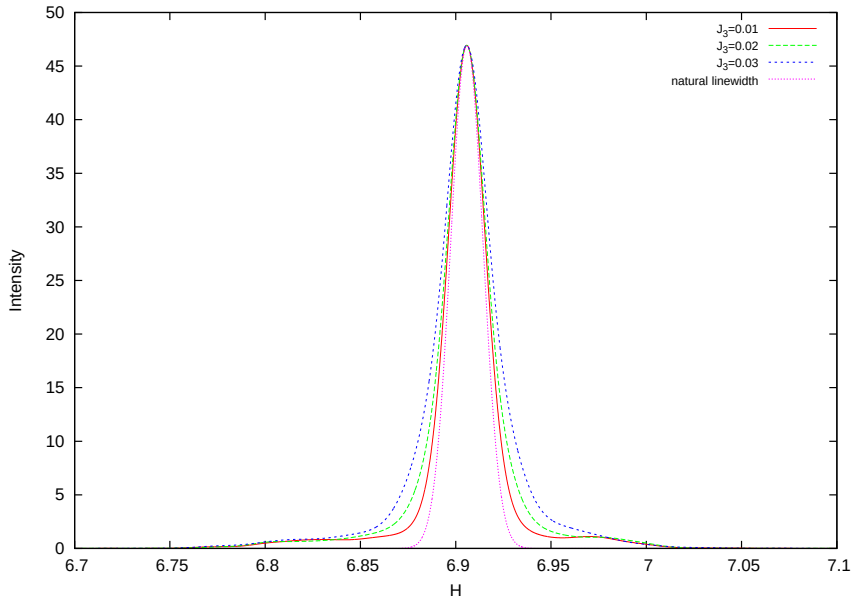

Figure 3.11: NMR profiles for $J_3/J_\parallel = 0.01, 0.02, 0.03$.

The measured correlation length for the 3D system ($J_3/J_\parallel = 0.01$) doesn't exceed $\xi = 8.5(5)$.

3.2.1 Correlation Length

Greven and Birgeneau [42] performed an analysis of the correlations in diluted spin ladders for different degrees of dilution. They measured the correlation length via the correlation functions in quantum Monte Carlo simulations. This approach is preferable because it can easily be done for many different vacancy configurations which can be averaged over. Greven et al. chose a number of configurations of 40 for each set of parameters.

A similar approach for the stacked ladder system was used here to determine correlation lengths in this system. For each determination 40 different vacancy configurations were chosen randomly. The equal time correlations in real space were calculated by Fourier transformation of the k-space correlations.

Systems of size $60 \times 2 \times 10$ with vacancy concentrations of 2% up to 7% were calculated at a temperature of $T = 0.015$ to compare it with the simple ladder system. The coupling strengths were set to the values proposed by Johnston et al. [1]: $J_\perp/J_\parallel = 0.5$, $J_3/J_\parallel = 0.01$.

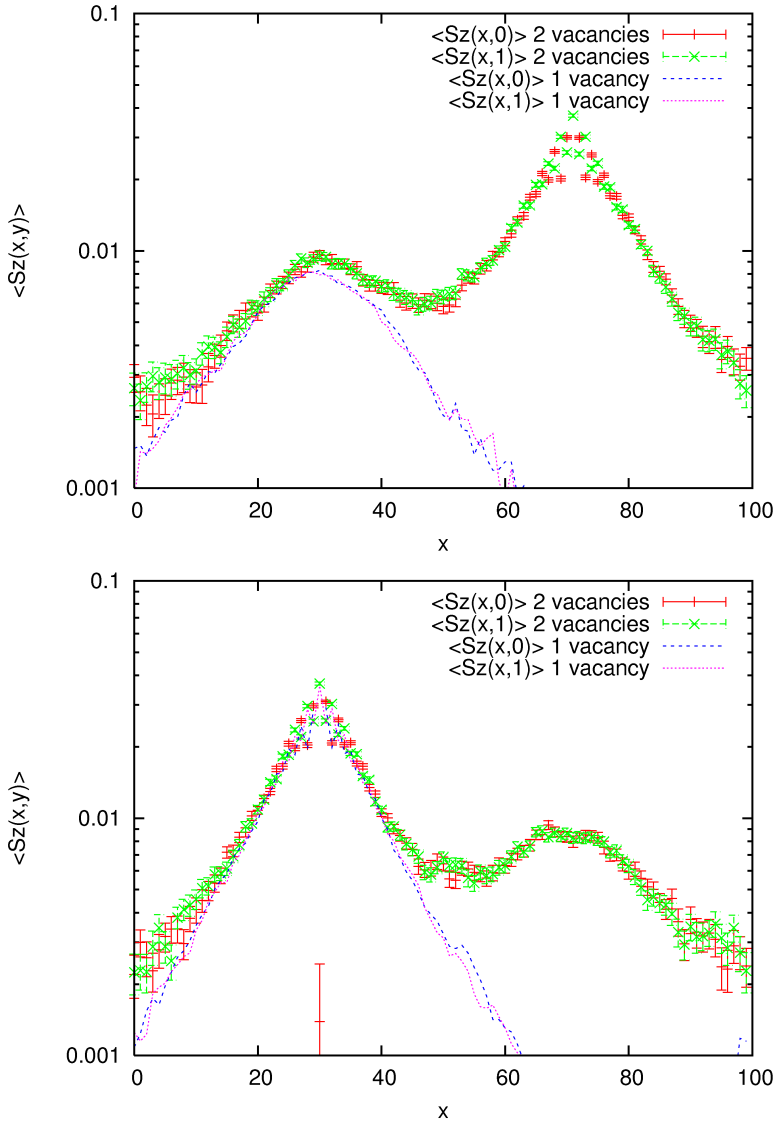

Figure 3.12: 2 vacancies on neighboring ladders, each picture corresponds to one of the stacked ladders. The coordinates of the vacancies are $(30, 0, 0)$ and $(70, 0, 1)$, $J_3/J_{\parallel} = 0.03$. For comparison magnetizations of a system with a single vacancy at $(30, 0, 0)$ are plotted, too.

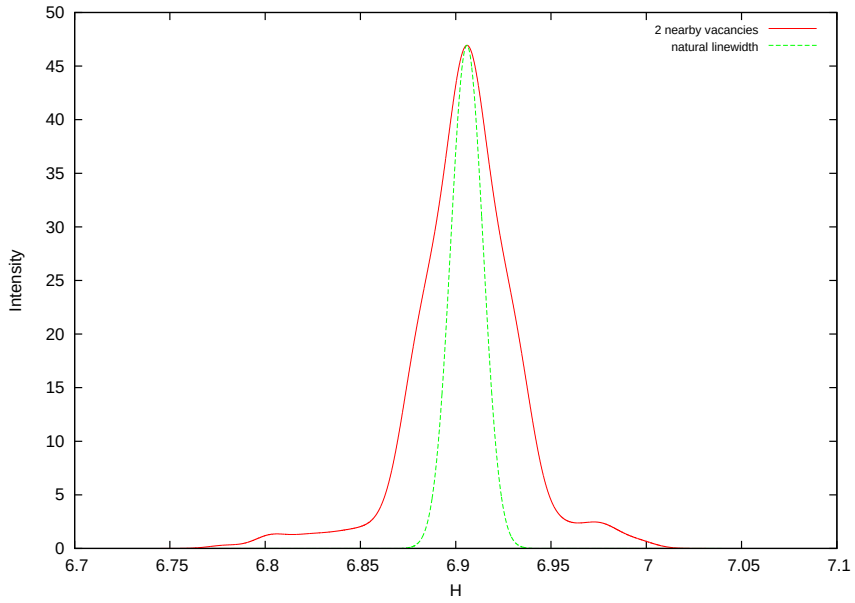

Figure 3.13: NMR spectrum of specific profile in fig. 3.12

Fig. 3.14 shows the real-space correlations in ladder-direction for a stacked ladder system as a function of distance. They are plotted for 40 different vacancy configurations. One can see the significant impact of the individual configurations primarily at the center of the picture.

To understand this behavior particularly for the center at distances of 30, the individual correlations of every lattice point with its corresponding lattice point of distance 30 in ladder direction have been calculated and are depicted in fig. 3.15 and 3.16. Each picture shows one of the coupled planes and the color code reflects the correlation strength. The large amount of correlations seen in the second picture emerges from the favorable positions of the vacancies in the lower half. Especially vacant sites on the same sublattice of distance 30 boost the correlations.

Every graph has been fitted with cosh-like model function to obtain the correlation lengths. The variance of the values is quite large due to the described strong dependence on the vacancy distribution. Figure 3.17 shows the resulting average correlation lengths for different vacancy densities.

The correlations might be increased by the presence of inter-ladder interactions. Unfortunately the quantity of the enlargement can't be told due to the large statistical error originating in computing limitations.

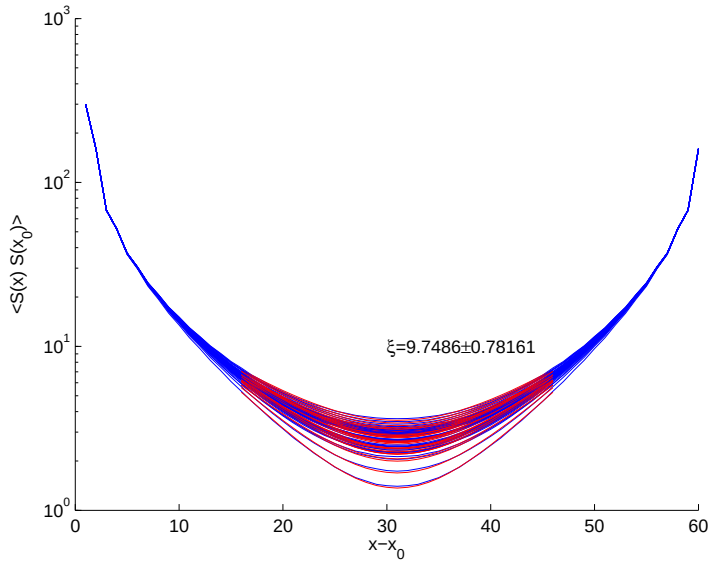

Figure 3.14: Real-space correlations as a function of distance for a $60 \times 2 \times 10$ system with 2% vacancy density. Shown are 40 different vacancy configurations. Additionally the cosh-fits for obtaining the correlation length are depicted. The resulting value $\xi = 9.75(78)$ is an average over all fitted correlation lengths.

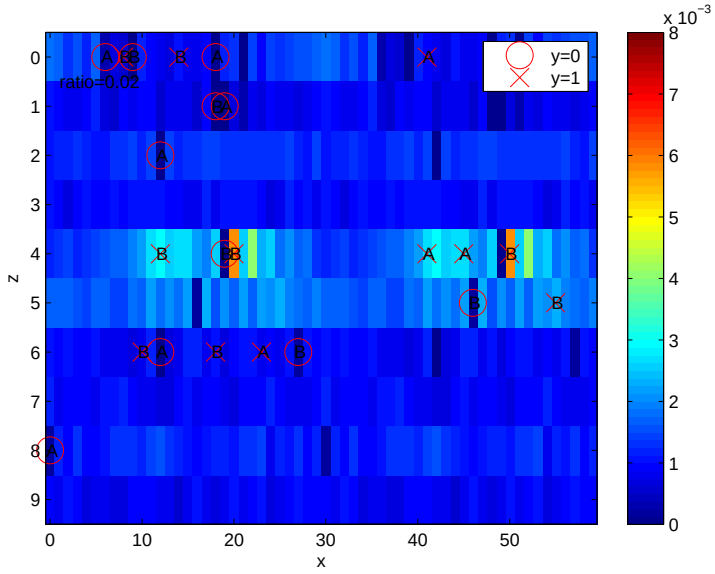

Figure 3.15: Correlations of each point of one of the coupled planes ($y = 0$) to its corresponding point of distance 30 in x-direction on a $60 \times 2 \times 10$-system with 2% vacancy density. The correlation strength is color-coded. Additionally the locations of the vacancies are shown and each of them is labeled with its corresponding sub-lattice (A or B). The configuration is the one with the lowest correlation strength in fig. 3.14.

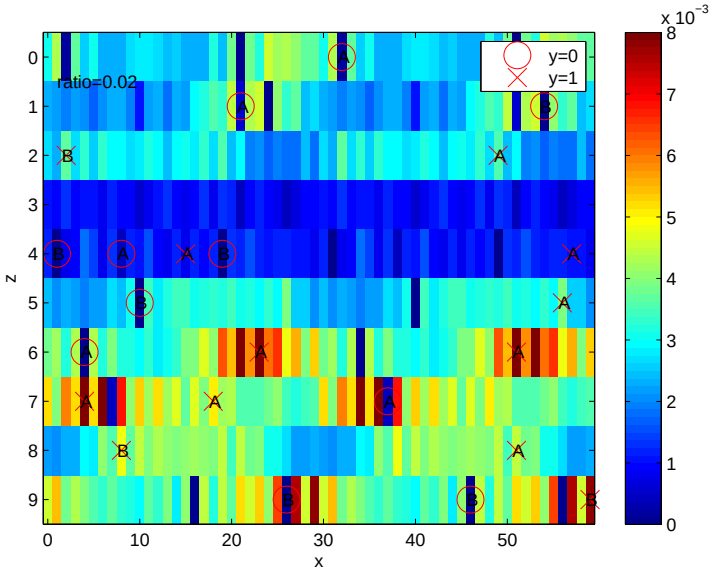

Figure 3.16: Correlations of each point of one of the coupled planes ($y = 0$) to its corresponding point of distance 30 in x-direction on a $60 \times 2 \times 10$-system with 2% vacancy density. The correlation strength is color-coded. Additionally the locations of the vacancies are shown and each of them is labeled with its corresponding sub-lattice (A or B). The configuration is the one with the largest correlation strength in fig. 3.14.

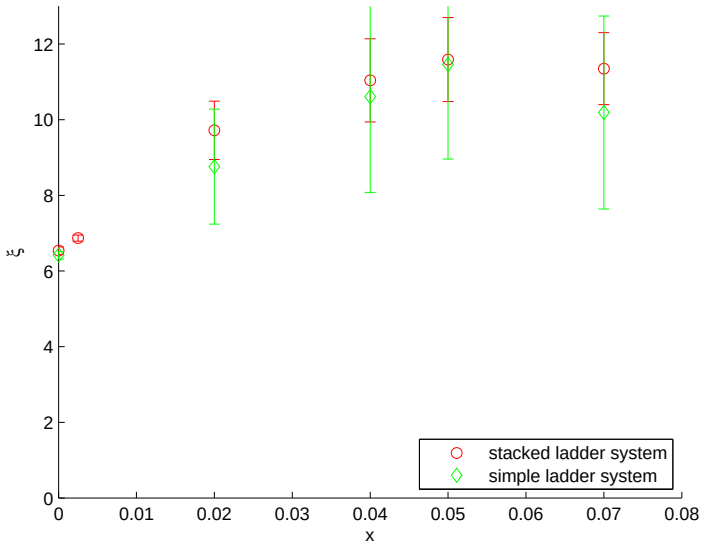

Figure 3.17: Correlation lengths as a function of vacancy density for the ladder system and the stacked ladder system.

3.3 Broadening Requirements

Putting the cart before the horse this section deals with the needs for correlation lengths to explain the broadening in the NMR experiments for stacked ladders (see sec. 1.6.1). By doing simple NMR simulations with exponential decay of local magnetizations and inputting different sets of correlation lengths in both ladder and stacking directions these requirements were estimated. An area-normalized plot turns out to be unfavorable compared to a maximum-normalized plot (see fig. 3.18). It includes refining of the parameters to approximate the experimental behavior of a line-width of about $800G$. One already sees that the needed correlation lengths for describing the experiments exceed the ones obtained in the simulations.
The corresponding domain of required values on the (ξ, ξ_3) plane is sketched in fig. 3.19. Furthermore some systems already calculated are drawn to get an overview over required coupling strengths. The values do not only exceed the values proposed by Johnston et al. (see sec. 1.4.1) by far, but one has to bear in mind, that some of the parameters define systems well inside the domain of the ordered phase. Furthermore the experimental data shows broadening only for samples with vacancies.

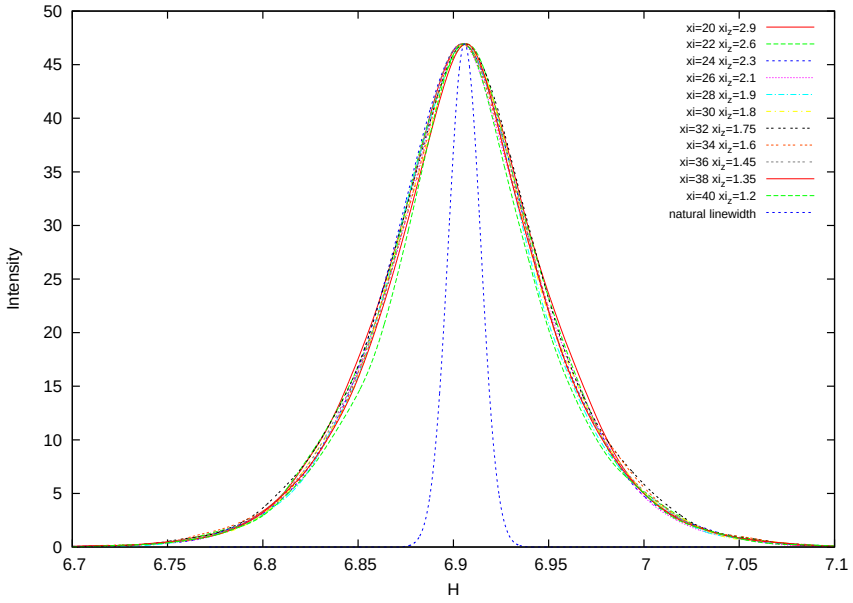

Figure 3.18: Requirements of correlation lengths for experimental line-width to explain the NMR data. Normalized to maximum.

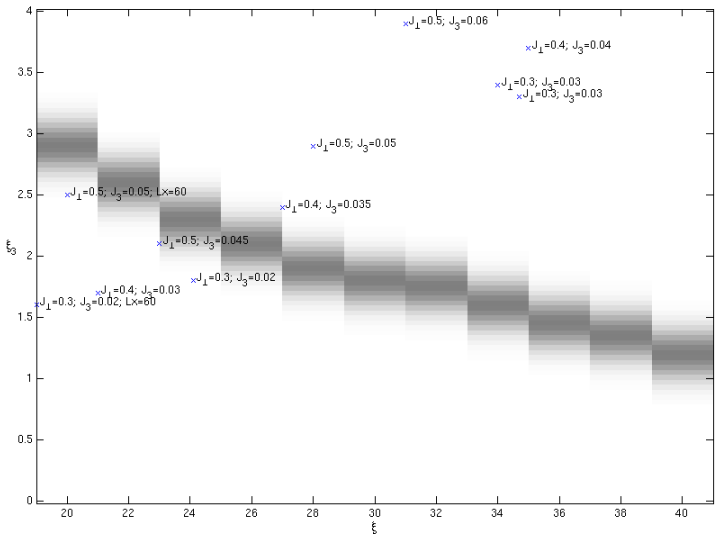

Figure 3.19: The required correlation lengths are depicted in shaded form. Additionally some simulations are drawn in with the coupling strengths used.

4 Conclusions

This thesis examined the influence of vacancies on spin-ladder systems with and without inter-ladder couplings, inspired by the material $SrCu_2O_3$. It was shown that near a vacancy a virtual spin is induced which is distributed in an area determined by the correlation length in the material (see sec. 2.1). This effect was confirmed observing the magnetization, excitation spectra (2.5), and correlational behaviour (2.6). The influence on simulations of NMR-spectra (2.2.3, 2.2.6) does not reproduce the drastic broadening seen at low temperatures in $SrCu_2O_3$. A proper description of this intriguing experimental observation will apparently require to go beyond the class of Heisenberg models employed in this thesis.

Also the effective interaction between the induced spins was examined with the help of the susceptibility (2.7). Further inter-ladder interactions like the diagonal (2.3) or cyclic exchange (2.4) terms were introduced. Their influence was either hardly existent or it changed the dynamics of the system in a way which is not consistent with the experiments. This is also true for the introduction of a spin anisotropy (2.8).

The system of stacked ladders exhibits a quantum phase transition, which was investigated by determining the critical coupling (3.1.3) as well as the critical exponents (3.1.5). The influence of vacancies on the stacked ladder system was shown by simulations for different impurity densities (3.2). Simulations of NMR spectra show the influence of vacancies on this system.

Acknowledgements

First of all I would like to thank Prof. Hans Gerd Evertz for his excellent guidance and supervision. Very special thanks go to DI Franz Michel who supported me in many ways and was never too bored or too annoyed to answer even the most impossible questions. I also want to thank Andreas Hirczy for providing the necessary computer infrastructure and Babette Hebenstreit for proof-reading. Furthermore I wish to thank the members of the many-particle physics group, Heinz-Georg Flesch, Danilo Neuber, Peter Pippan, Ingrid Reiweger, Christian Scheiber, and Martin Schmierdorfer.

Bibliography

[1] D. C. Johnston *et al.*, Magnetic Susceptibilities of Spin-1/2 Antiferromagnetic Heisenberg Ladders and Applications to Ladder Oxide Compounds, cond-mat/0001147, 2000.

[2] C. J. Calzado *et al.*, Phys. Rev. B **67**, 132409 (2003).

[3] N. Fujiwara *et al.*, Phys. Rev. Lett. **80**, 604 (1998).

[4] S. Ohsugi *et al.*, Phys. Rev. B **60**, 4181 (1999).

[5] M. Azuma, M. Takano, and R.S.Eccleston, Journal of the Physical Society of Japan **67**, 740 (1998).

[6] M. Azuma *et al.*, Phys. Rev. B **55**, R8658 (1997).

[7] `http://hiroi.issp.u-tokyo.ac.jp/`.

[8] H. Bethe, Zeitschrift für Physik A **71**, 205 (1931).

[9] M. Greven, R. J. Birgeneau, and U. J. Wiese, Phys. Rev. Lett. **77**, 1865 (1996).

[10] G. Sierra, On the Application of the Non Linear Sigma Model to Spin Chains and Spin Ladders, 1997.

[11] T. Giamarchi, *Quantum Physics in One Dimension* (Oxford Science Publications, Oxford, 2004).

[12] P. Henelius and A. W. Sandvik, Phys. Rev. B **62**, 1102 (2000).

[13] H.-J. Mikeska, U. Neugebauer, and U. Schollwöck, Phys. Rev. B **55**, 2955 (1997).

[14] J. Binney, N. Dowrick, A. Fisher, and M. Newman, *The Theory of Critical Phenomena* (Oxford University Press, Oxford, 1992).

[15] G. Czycholl, *Theoretische Festkörperphysik* (Vieweg, Braunschweig/Wiesbaden, 2000).

[16] T. S. Nunner *et al.*, Phys. Rev. B **66**, 180404 (2002).

[17] Y. Motome, N. Katoh, N. Furukawa, and M. Imada, Journal of the Physical Society of Japan **65**, 1949 (1996).

[18] Y. Mizuno, T. Tohyama, and S. Maekawa, Phys. Rev. B **58**, R14713 (1998).

[19] M. Laukamp *et al.*, Phys. Rev. B **57**, 10755 (1998).

[20] C. Weißmantel and C. Hamann, *Grundlagen der Festkörperphysik* (Johann Ambrosius Barth Verlag, Heidelberg/Leipzig, 1995).

[21] F. Tedoldi, R. Santachiara, and M. Horvatić, Phys. Rev. Lett. **83**, 412 (1999).

[22] M. Azuma *et al.*, Phys. Rev. Lett. **73**, 3463 (1994).

[23] K. Ishida *et al.*, Journal of the Physical Society of Japan **63**, 3222 (1994).

[24] Ishida *et al.*, Phys. Rev. B **53**, 2827 (1996).

[25] N. Metropolis *et al.*, The Journal of Chemical Physics **21**, 1087 (1953).

[26] H. G. Evertz, Advances in Physics **52**, 1 (2003).

[27] A. W. Sandvik and J. Kurkijärvi, Phys. Rev. B **43**, 5950 (1991).

[28] M. Troyer, F. Alet, S. Trebst, and S. Wessel, AIP conf.proc. **690**, 156 (2003).

[29] A. W. Sandvik and O. F. Syljuåsen, in *The Directed-Loop Algorithm*, edited by J. E. Gubernatis (AIP, Los Alamos, New Mexico (USA), 2003), No. 1, pp. 299–308.

[30] `http://alps.comp-phys.org`.

[31] F. Michel, *Quantum Monte Carlo Simulations for Spin and Spin-Phonon Simulations* (Graz University of Technology, Graz, 2006).

[32] W. Nolting, *Grundkurs Theoretische Physik 7 Viel-Teilchen-Theorie* (Vieweg, Braunschweig/Wiesbaden, 1997).

[33] U. Schollwöck, Reviews of Modern Physics **77**, 259 (2005).

[34] P. Pippan, *The Density Matrix Renormalisation Group and Matrix Product States* (Graz University of Technology, Graz, 2006).

[35] W. Linden and A. Prüll, *Wahrscheinlichkeitstheorie, Statistik und Datenanalyse* (lecture notes, Graz, 2002).

[36] O. A. Starykh, A. W. Sandvik, and R. R. P. Singh, Phys. Rev. B **55**, 14953 (1997).

[37] M. Vojta, C. Buragohain, and S. Sachdev, Phys. Rev. B **61**, 15152 (2000).

[38] A. W. Sandvik and D. J. Scalapino, Phys. Rev. Lett. **72**, 2777 (1994).

[39] P. Sengupta, W. Zheng, and R. R. P. Singh, Phys. Rev. B **69**, 064428 (2004).

[40] A. W. Sandvik, Phys. Rev. Lett. **83**, 3069 (1999).

[41] A. W. Sandvik, Phys. Rev. B **56**, 11678 (1997).

[42] M. Greven and R. J. Birgeneau, Phys. Rev. Lett. **81**, 1945 (1998).